TIME-DOMAIN POLARIZATION-SENSITIVE OPTICAL COHERENCE TOMOGRAPHY IN SOFT BIOLOGICAL TISSUE

A Dissertation

by

MILOS TODOROVIC

Submitted to the Office of Graduate Studies of
Texas A&M University
in partial fulfillment of the requirements for the degree of

DOCTOR OF PHILOSOPHY

August 2008

Major Subject: Biomedical Engineering

TIME-DOMAIN POLARIZATION-SENSITIVE OPTICAL COHERENCE TOMOGRAPHY IN SOFT BIOLOGICAL TISSUE

A Dissertation

by

MILOS TODOROVIC

Submitted to the Office of Graduate Studies of
Texas A&M University
in partial fulfillment of the requirements for the degree of

DOCTOR OF PHILOSOPHY

Approved by:

Co-Chairs of Committee,	Lihong V. Wang
	Gerard L. Cote
Committee Members,	Gheorghe Stoica
	Alvin T. Yeh
Head of Department,	Gerard L. Cote

August 2008

Major Subject: Biomedical Engineering

ABSTRACT

Time-Domain Polarization-Sensitive Optical Coherence Tomography in Soft Biological Tissue. (August 2008)

Milos Todorovic, B.S., University of Belgrade;

M.S., Texas A&M University

Co-Chairs of Advisory Committee, Dr. Lihong V. Wang
Dr. Gerard L. Cote

A new, high-speed, fiber-based Mueller-matrix optical coherence tomography system with continuous source-polarization modulation is presented. For *in vivo* experimentation, the sample arm optics are integrated into a hand-held probe. The system's parameters were verified through imaging standard optical elements. A unique feature of polarization-sensitive Mueller optical coherence tomography is that by measuring Jones or Mueller matrices, it can reveal the complete polarization properties of biological samples, even in the presence of diattenuation. Presented here for the first time are mapped local polarization properties of biological samples obtained by using polar decomposition in combination with least-squares fitting to differentiate measured integrated Jones matrices with respect to depth. In addition, a new concept of dual attenuation coefficients to characterize diattenuation per unit infinitesimal length in tissues is introduced. The algorithm was experimentally verified using measurements of a section of porcine tendon and the septum of a rat heart.

The application of the system for burn imaging and healing monitoring was demonstrated on porcine skin because of its similarity to the human skin. The results showed a clear localization of the thermally damaged region. The local birefringence of the *intravital* porcine skin was mapped by using a differentiation algorithm. The burn areas in the OCT images agree well with the histology, thus demonstrating the system's potential for burn-depth determination and post-injury healing monitoring.

Another major application of the fiber-based Mueller-matrix optical coherence tomography system with continuous source-polarization modulation covered here is *in vivo* imaging of early stages of skin cancer. The OCT images of SENCAR mice skin affected by the tumorigenesis show the structural changes in skin resulting from pre-cancerous papilloma formations that are consistent with histology, which proves the system's potential for early skin cancer detection.

DEDICATION

To Maja and Ema for their love, support and understanding during this journey

and

To my parents for sparking the fire of curiosity that is still strongly burning.

ACKNOWLEDGEMENTS

The utmost gratitude goes to the members of my committee. This work would not have been possible without their support. I would especially like to thank Dr. Cote for his encouragement during hard times and for believing in me even when I doubted myself. Also, a special thanks goes to Dr. Stoica for introducing me to the wonderful world of medicine and all the intricacies of physiology.

I would also like to thank Dr. Meissner from the Department of Biomedical Engineering at Texas A&M University for long discussions and willingness to help even in the hardest of situations.

The help of my fellow lab mates, Sava Sakadžić and David Pereda-Cubián, was instrumental in broadening my horizons and making long days in the lab more bearable. A big thanks goes to all other members of the Optical Imaging Lab, too.

Finally, I would like to acknowledge the support of the Department of the Army (Cooperative Agreement Number: DAMD17-97-2-7016) and the National Institutes of Health (R01 CA092415).

TABLE OF CONTENTS

CHAPTER Page

LIST OF FIGURES

Page

CHAPTER I

INTRODUCTION

1. Motivation for research

Optical imaging of soft biological tissue is highly desirable due to its non-ionizing nature, excellent resolution, and its ability to provide sensitive contrast information which enables, among other things, potential early cancer detection [1], burn injury assessment [2, 3], and functional imaging at cellular level [4]. To stress the importance of the need for optical imaging note that the current techniques for, for example, cancer detection (ultrasound, x-ray computerized tomography, and magnetic resonance imaging) are not very efficient in detecting lesions smaller than ~1 cm. As a result, most of the cancers detected by these methods are in advanced stages, and development of new techniques for early cancer detection is an imperative.

The optical properties of soft biological tissues in the visible and near-infrared regions of the optical spectrum are related to the molecular and cellular structure, offering potential for the investigation of tissue morphology (optical biopsy), physiology and pathology. For example, cancer-related tissue abnormalities, such as angiogenesis, hyper-metabolism, and invasion into adjacent normal tissue, possess optical signatures (polarization, scattering and absorption) that offer the potential for early cancer detection.

This dissertation follows the style of Optics Express.

The optical scattering and polarization properties of tissue are strongly related to the tissue structure (e.g. cell nuclei size, shape and density). On the other hand, optical absorption properties can reveal metabolic processes (hemoglobin concentration and oxygen saturation) and angiogenesis. However, due to the strong scattering of light in biological tissue, optical imaging at imaging depths greater than one optical transport mean free path (~1 mm in soft biological tissues at visible and near-infrared wavelengths) presents a challenge.

Optical coherence tomography (OCT) has been developed to measure depth-resolved images of various biological tissues [5]. With respect to penetration depth (up to 2 mm) and axial resolution (up to 1 micron) it falls somewhere between confocal and fluorescence-based multi-photon microscopy (penetration depth: few hundred microns; resolution: several hundred nanometers [4]) on one end and hybrid ultrasound/optical techniques such as photo-acoustic tomography (PAT) and ultrasound-modulated optical tomography (UOT) (penetration depth: few millimeters; resolution: ~ 150 microns at 10 MHz US frequency [1]) on the other end of the optical imaging spectrum. Due to the limited penetration depth when compared with modalities capable of full body imaging (X ray-based technologies, MRI), the optical imaging systems mainly focus on applications in skin, body cavities and other organs and tissues within several millimeters below the surface for *in vivo* applications. Although the multi-photon fluorescence microscopy and similar imaging modalities can achieve better resolution than OCT, their application is limited by the penetration depth. For example, the average human skin thickness is between 1 mm and 2 mm depending on the site [6] and majority

of lesions that can develop in skin spread well below the 400-500 micron penetration depth limit of these technologies. On the other hand, PAT and UOT can image several times deeper than OCT but their axial resolution, although scalable with US frequency, is approximately two orders of magnitude worse. High resolution imaging is essential for early detection of any abnormalities that may develop in tissues and for functional imaging at cellular level.

It can be seen that OCT provides a nice balance of very good resolution and fairly large penetration depth in soft biological tissues. While the penetration depth is limited by the strong scattering in biological samples and will remain the strongest impediment to deep tissue imaging with OCT, the development of ultra-wide broadband light sources has a potential to further enhance the resolution of OCT systems and extend their use to sub-cellular level imaging.

In addition to the intensity contrast due to the changes in the index of refraction, a special branch of OCT called polarization-sensitive OCT (PS-OCT) is capable of visualizing the polarization contrast stemming from optical polarization properties of samples, such as birefringence (with its phase retardation and orientation) and diattenuation (magnitude and orientation) [7-9].

Several methods have been developed to exploit the polarization contrast with the PS-OCT. When the optical system is constructed in free space, the orientation and the phase retardation of the birefringence of the sample can be directly obtained from two orthogonally polarized phase resolved signals of the time-domain PS-OCT (PS-TD-OCT) [10]. This method was extended to Fourier-domain OCT (FD-OCT) [11], because

the FD-OCT enables faster imaging and higher signal-to-noise ratio as compared to the TD-OCT [12, 13]. Another TD-OCT method using the Stokes vector [14] can be used to visualize the changes in the polarization on the Poincaré sphere. Fiber-based PS-OCT was first demonstrated by Saxer *et al.* with the Stokes vector method [15]. This method has also been demonstrated with swept-source OCT [16] and FD-OCT [17]. Mueller matrix, which can describe the complete polarization property of a sample, was first measured with OCT by Yao *et al.* [18]. Yasuno *et al.* first demonstrated polarization-sensitive FD-OCT (PS-FD-OCT) using the Mueller matrix method [19].

Birefringence contrast describes the anisotropy of the phase velocity of light in a sample which is inherent in a variety of biological components. Diattenuation contrast describes the anisotropy of the transmittance in a sample and is also present in biological tissues, although it is usually less pronounced than birefringence. However, the potential of birefringence and diattenuation contrasts for determining the depth-resolved local polarization properties and the structures of samples has not been fully exploited due to the integrating nature of phase retardation and attenuation (and consequently transmittance) along the optical path. The integrating nature of these parameters diminishes the polarization contrast due to the fact that polarization properties of tissue segments laying further down the optical axis can be masked by strongly pronounced phase retardation or attenuation of preceding segments. Therefore, the need for an algorithm that is capable of extracting the polarization parameters of small segments at all depths along the axial scans (A-scans) in the sample is evident. Another requirement of such algorithm is to be robust enough to yield correct values even when the

orientation of the fast optical axis of the sample is non-uniform, i.e. when it changes its orientation along the optical path.

2. Research objectives

The research presented in this dissertation was based on three main objectives: 1. development of a high-speed fiber-based time-domain Mueller-OCT system for high-resolution imaging of soft biological tissues; 2. characterization of the capabilities of the developed hand-held probe equipped system and understanding the origin of OCT polarization contrast by imaging various biological tissue samples *ex vivo* and skin cancers and burns in animal models *in vivo*; and 3. development of an algorithm that would allow extraction of localized (depth differentiated) polarization properties of soft biological tissue from measured round trip Jones matrices, even in the presence of diattenuation. The work was carried out in several phases as outlined in the next several subchapters.

2.1. Objective 1

To measure a Jones matrix, usually at least two incident polarization states and two detection channels are needed [20]. Two incident polarization states can be applied either simultaneously or sequentially. Simultaneous application requires using two differently polarized independent light sources. Different incident polarization states using only one light source can be applied sequentially by varying the source polarization state with optical polarization elements [15, 21]. The former method has an

advantage in imaging speed as it can measure the Jones matrix of a sample with a single measurement. The advantage of the sequential implementation is that only one light source is needed. However, the sequential approach requires multiple depth scans (A-scans) to calculate the Jones matrix. As a result, a system that can combine the advantages of both of these configurations is highly desirable. To ensure that the information acquired with a single measurement is sufficient for the calculation of the Jones matrix of a sample, one approach is to modulate the source polarization state continuously [22]. The high-speed fiber-based PS-OCT system presented here is based on this approach. The incident light polarization is continuously modulated using the electro-optical modulator. The modulation frequency has to be high enough to ensure that multiple cycles of polarization states are applied to each segment of a depth scan (A-scan).

To facilitate the *in vivo* imaging, it is much more convenient if the sample arm is built using single mode fibers. To ensure the minimum group velocity dispersion between the reference and sample arm, and thus ensure the optimal longitudinal resolution, attention was given to proper fiber length matching between the arms. Additional sources of dispersion can be found in bulk optics so the goal should be to match the optical pathlengths in lenses in both arms of the system. To further aid the *in vivo* imaging a hand-held probe was built, which made the sample arm mobile. The hand-held probe integrates a collimating lens, B-scan mirror and a focusing lens of the sample arm.

2.2. Objective 2

Polarization contrast exists in various soft biological tissues and is found to be an important parameter for their characterization [23, 24]. Collagen is a predominant structural component in many of those biological tissues and is known to be birefringent. For example, the most abundant family of proteins in the extracellular matrix is the collagens with more than 20 different collagen types identified so far [25]. Collagens are centrally involved in the formation of fibrillar and microfibrillar networks of the extracellular matrix, basement membranes as well as other structures of the extracellular matrix and, as such, they define structural integrity and various physiological functions. Collagens are known to possess both the intrinsic and form birefringence. The intrinsic birefringence is related to the spatial arrangement of atomic groups and molecules. The intensity of intrinsic birefringence is mainly a function of the alignment and order of the molecular packaging, but also of the nature of the chemical groups encountered. Form birefringence occurs in rod-like and plate-like structures immersed in a medium having a different refractive index. The observed birefringence is the overall effect of these two types of birefringence.

Also, the elongated, asymmetrical shape of muscle fibers in general suggests the presence of a fast optical axis [26]. However, the actual source of birefringence in skeletal muscle is highly dependent on biological, physiological, and environmental conditions. A series of light and dark “bands” perpendicular to the long axis of the muscle fiber appear when imaging both skeletal and cardiac muscle fibers through a light microscope. The presence of these bands or striations is due to the arrangement of

thick (myosin) and thin (actin) filaments in the myofibrils of the muscle cell. The light and dark bands are referred to as A-bands (anisotropic) and I-bands (isotropic), respectively. The myosin filaments in the A bands are considered to be the anisotropic source of form birefringence present in muscle tissue. Therefore, as the presence and organization of thick filaments in muscle type varies, so does the overall birefringence of the tissue.

In addition to morphology of tissues, pathological processes can contribute to the polarization contrast. It is known that, for example, thermal damage to skin causes the destruction of collagen structures, which in turn reduces the overall birefringence of the exposed region. Cancers also have a diverse effect on the polarization properties of affected tissue. Due to the fast and often chaotic growth of cancers, they tend to disrupt the natural organization of fibrillar structures, which also has a potential to reduce the form birefringence.

My research exploits the ability of PS-OCT to characterize the polarization properties of soft biological tissues to investigate the polarization of various specimens and pathological conditions. In particular, the research focuses on using the system to locate and monitor the growth of skin cancers in the animal model (SENCAR mice). Also, the particular attention is given to assessing the extent of burn injuries and temporal monitoring of the healing process. This part of the study used a pig skin as the specimen due to its similarities with human skin.

2.3. Objective 3

The Jones matrix for a given depth along each A-scan encompasses the integrated effect of all of the segments within the depth. Algebraically, we can recover any round-trip single-segment matrix by recovering the one-way single-segment matrices of the preceding segments one-by-one and eliminating their integrating effects.

In order to implement this approach a model of a tissue segment was assumed to proceed with characterizing its properties. A sequence of a linear diattenuator and a linear retarder can model a thin segment of biological tissue well. This model is reasonable because physical properties, such as the orientation of the collagen fibers, are almost constant at the scale of the resolution of the OCT system (~10 μm). A further assumption was made that the orientations of the retarder and diattenuator are the same, which is logical since their orientations are directly related to the orientation of the tissue fibers. In this case, the order between the diattenuator and retarder is irrelevant and the thin tissue segment can be referred to as homogeneous in the sense of polarimetry.

Once the tissue optical model is defined and the overall round-trip Jones matrix of the segment is measured, the polar decomposition theorem can be applied to calculate the characteristic parameters of the retarder and diattenuator (phase retardation – φ, orientation – θ and transmittances of the fast and slow eigenvectors – p_x and p_y, respectively). The polar decomposition theorem, when used with Jones matrices, states that any nondepolarizing polarization element described by a Jones matrix can be represented as a cascade of a diattenuator and a retarder [27]. The polar decomposition yields two matrices – a unitary matrix U corresponding to a retarder and a nonnegative

definite Hermitian matrix H corresponding to a diattenuator. To calculate the parameters of an individual segment, matrices U and H can be fit to the model Jones matrices of a linear retarder and linear diattenuator in the least-squares sense, respectively. The motivation for using the least-squares approach is to take advantage of the fact that mathematical expressions for all four elements of the model Jones matrix contain all characteristic parameters (φ, θ, p_x, and p_y). This statistical approach aids the robustness of the algorithm.

3. Dissertation outline

Following this introductory chapter, the dissertation continues with the introduction of the high-speed PS-OCT system in Chapter II. Chapter III presents the differentiation algorithm used to extract localized polarization properties of samples. This is followed by Chapter IV, which shows the results of the burn imaging study and Chapter V, which presents the results of the effort to detect skin cancer in SENCAR mouse model in the early stages of tumorigenesis. Finally, the dissertation concludes with an overview of the work in Chapter VI.

CHAPTER II

TIME-DOMAIN POLARIZATION-SENSITIVE OPTICAL COHERENCE TOMOGRAPHY SYSTEM

1. Introduction

To measure a Jones matrix, usually at least two incident polarization states and two detection channels are needed [20]. Two incident polarization states can be applied either simultaneously or sequentially. Simultaneous application requires using two differently polarized independent light sources. Different incident polarization states using only one light source can be applied sequentially by varying the source polarization state with optical polarization elements [15, 21]. The former method has an advantage in imaging speed as it can measure the Jones matrix of a sample with a single measurement. The advantage of the sequential implementation is that only one light source is needed. However, the sequential approach requires multiple depth scans (A-scans) to calculate the Jones matrix. As a result, a system that can combine the advantages of both of these configurations is highly desirable. To ensure that the information acquired with a single measurement is sufficient for the calculation of the Jones matrix of a sample, one approach is to modulate the source polarization state continuously [22]. The high-speed fiber-based PS-OCT system presented in this chapter is based on this approach. The incident light polarization is continuously modulated using the electro-optical modulator. The modulation frequency has to be high enough to

ensure that multiple cycles of polarization states are applied to each segment of a depth scan.

2. Experimental system

The schematic of the polarization-sensitive Mueller-matrix OCT system is shown in Figure 2.1. Light from a broadband super-luminescent diode (SLD)-based light source (Superlum; λ_0 = 1.3 μm, FWHM-BW = 60 nm, output power 10 mW) is vertically polarized. A polarization modulator (Conoptics; fast axis at 45º) continuously modulates the source-polarization state with a 140 kHz sinusoidal waveform. The incident light beam is split by the non-polarizing beam splitter and light is delivered to the reference and the sample arm through single-mode optical fibers. A linear polarizer, oriented at -45º, is placed at the input of the reference arm to control the reference light polarization state.

A grating-based rapid scanning optical delay (RSOD) line [28] is used for longitudinal scanning. A collimating lens, B-scan mirror and focusing lens in the sample arm are integrated into a hand-held probe to facilitate *in-vivo* imaging. Due to the fact that light beam in the RSOD traverses the lens four times, as opposed to only two times in the sample arm, BK7 prisms are used in the sample arm for dispersion compensation. In addition to dispersion compensation, BK7 prisms are also used for beam height adjustment because the entrance of the sample arm is at the higher level above the optical table than the rest of the system. This height difference is necessitated by the need for multiple degrees of freedom for sample arm positioning.

The combined backreflected sample and reference light is split into horizontal and vertical polarization components by a polarizing beam splitter and detected by two photodiodes. Scanning galvanometers (Cambridge Technology) in the reference and sample arms are driven by triangular waves generated using two function generators (Stanford Research Systems). A 12-bit DAQ card (National Instruments) is used to digitize the detected analog signal for computer processing. The entire setup is controlled through a LabView-based graphical user interface (GUI) running on a PC computer. Communication between the computer and instruments is established over the GPIB bus. The synchronization of the system was achieved by distributing a unique trigger signal to all instruments.

Given the band-limited equipment (filters and data acquisition board), we selected the components of the interference signals at the lowest frequencies to calculate the Jones matrix elements. Those are the terms at the carrier frequency (90 kHz) and the beating frequency (50 kHz). It is important that the polarization modulator not be saturated at any point.

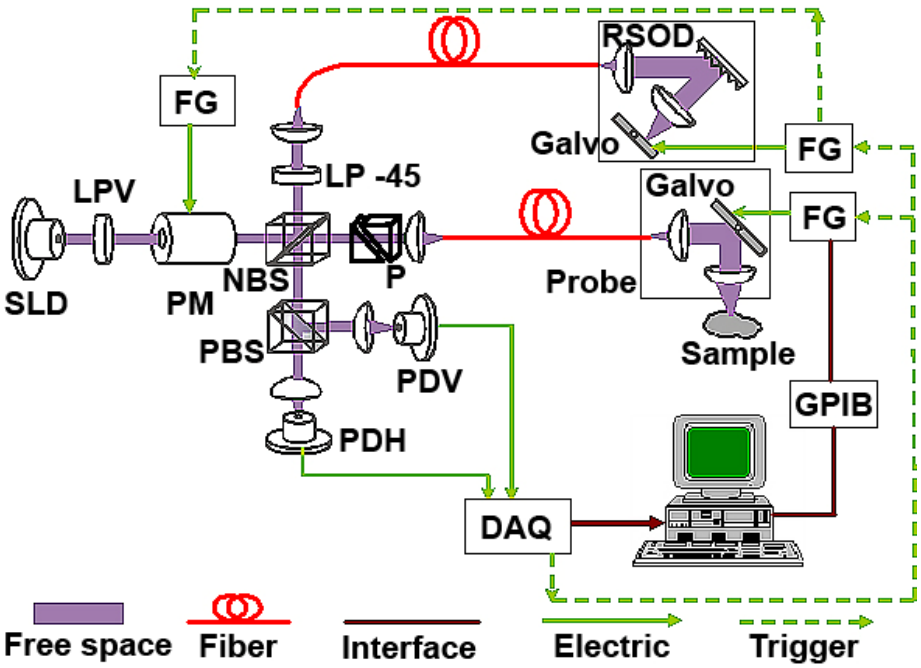

Fig. 2.1. Schematic of the Mueller PS-OCT system. SLD, super-luminescent diode; PM, polarization modulator; NBS, non-polarizing beam splitter; PBS, polarizing beam splitter; PDH, PDV, photodiodes for horizontal and vertical polarization, respectively; RSOD, rapid scanning optical delay line; LPV, vertical linear polarizer; LP -45, -45º linear polarizer; P, BK7 glass prisms; FG, function generator; DAQ, data acquisition block.

Figure 2.2 shows the photographs of the entire system (a) and the hand-held probe (b). The hand-held probe is shown attached to the post, which is a setup used for imaging smaller samples. When performing *in vivo* imaging of larger animals, the probe is taken off the post and can be freely moved in the radius of 1 m (the length of the single mode optical fiber).

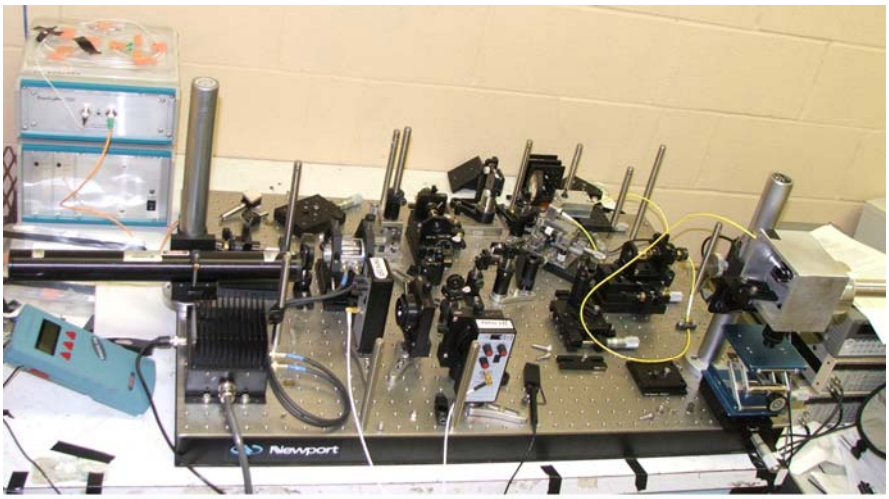

(a)

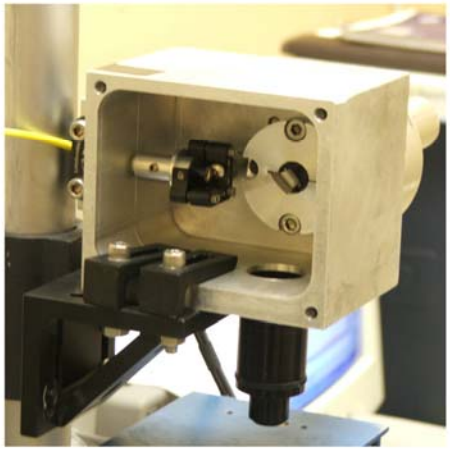

(b)

Fig. 2.2. Photographs of the entire PS-OCT system (a) and the hand-held probe (b).

3. Formulae for calculation of Jones matrix elements

Light emerging from the SLD-based light source is not polarized. The vertical linear polarizer polarizes the beam and the emerging light is considered the input to the rest of the system. Input Jones vector represents vertically polarized light:

$$E_{in} = \begin{bmatrix} 0 \\ 1 \end{bmatrix} \tag{2.1}$$

The Jones matrix of the polarization modulator is that of a linear retarder oriented at 45^{o} and is given by:

$$J_{pm} = \begin{bmatrix} \cos(\varphi/2) & i\sin(\varphi/2) \\ i\sin(\varphi/2) & \cos(\varphi/2) \end{bmatrix} \tag{2.2}$$

where φ is the constantly modulated phase. The light coming out of the modulator is described by the following Jones vector:

$$E_{pm} = J_{pm}E_{in} = \begin{bmatrix} i\sin(\varphi/2) \\ \cos(\varphi/2) \end{bmatrix} \tag{2.3}$$

General form of the round-trip Jones matrix of the sample arm is

$$J_{rt\_sample} = \begin{bmatrix} J_{11} & J_{12} \\ J_{21} & J_{22} \end{bmatrix} \tag{2.4}$$

and it encompasses the effects of the single mode fiber and all bulk optics in the sample arm. The Jones vector of the light emerging from the sample arm is then:

$$E_{sample} = J_{rt\_sample} E_{pm} = \begin{bmatrix} iJ_{11}\sin(\varphi/2) + J_{12}\cos(\varphi/2) \\ iJ_{21}\sin(\varphi/2) + J_{22}\cos(\varphi/2) \end{bmatrix} \tag{2.5}$$

The output of the reference arm, which has a linear polarizer oriented at -45^o at its input, is given by the following Jones vector:

$$\begin{aligned} E_{ref} &= J_{rt\_reference} E_{pm} \\ &= \frac{1}{4}\begin{bmatrix} 1 & -1 \\ -1 & 1 \end{bmatrix}\begin{bmatrix} J_{rt\_ref11} & J_{rt\_ref11} \\ J_{rt\_ref11} & J_{rt\_ref11} \end{bmatrix}\begin{bmatrix} 1 & -1 \\ -1 & 1 \end{bmatrix}\begin{bmatrix} i\sin(\varphi/2) \\ \cos(\varphi/2) \end{bmatrix} \\ &= \frac{1}{4}\begin{bmatrix} \left(J_{rt\_ref11} - J_{rt\_ref12} - J_{rt\_ref21} + J_{rt\_ref22}\right)\left(i\sin(\varphi/2) - \cos(\varphi/2)\right) \\ -\left(J_{rt\_ref11} - J_{rt\_ref12} - J_{rt\_ref21} + J_{rt\_ref22}\right)\left(i\sin(\varphi/2) - \cos(\varphi/2)\right) \end{bmatrix} \\ &= E_{ref}\begin{bmatrix} -1 \\ 1 \end{bmatrix} e^{-i\varphi/2} = \begin{bmatrix} E_{refH} \\ E_{refV} \end{bmatrix} e^{-i\varphi/2} \end{aligned} \tag{2.6}$$

It can be seen that the light emerging from the reference arm has equal amplitudes in both vertical and horizontal polarization state and that the electric field vectors are phase shifted by 180^o. It is also obvious that the horizontally and vertically polarized component intensities emerging from the reference arm and detected with photo-detectors are constant, regardless of polarization modulation. This fact can be used for the alignment of the polarization modulator because the above holds true only if the modulator is oriented at 45^o.

The light in the detection arm is a sum of two beams coming from the reference and sample arms and can be characterized by the following Jones vector:

$$E_{combined} = E_{sample} + E_{ref} = \begin{bmatrix} iJ_{11}\sin(\varphi/2) + J_{12}\cos(\varphi/2) + E_{refH}e^{-i\varphi/2} \\ iJ_{21}\sin(\varphi/2) + J_{22}\cos(\varphi/2) + E_{refV}e^{-i\varphi/2} \end{bmatrix} \tag{2.7}$$

The electric field incident on the photo-detectors in the vertical and horizontal polarization state is:

$$\begin{aligned} E_H &= \begin{bmatrix} iJ_{11}\sin(\varphi/2) + J_{12}\cos(\varphi/2) + E_{refH}e^{-i\varphi/2} \\ 0 \end{bmatrix} \\ E_V &= \begin{bmatrix} 0 \\ iJ_{21}\sin(\varphi/2) + J_{22}\cos(\varphi/2) + E_{refH}e^{-i\varphi/2} \end{bmatrix} \end{aligned} \tag{2.8}$$

The current induced in the photo-detectors is proportional to the intensity of the incident light. The corresponding intensities are:

$$\begin{aligned} I_H &= \mathrm{Re}\left\{E_H^{\otimes} E_H\right\} \\ I_V &= \mathrm{Re}\left\{E_V^{\otimes} E_V\right\} \end{aligned} \tag{2.9}$$

where $\otimes$ represents the complex conjugate transpose. As a result of the above multiplications, the light intensity will have DC and AC components. Only the AC component contributes to the interference fringes and those components in the vertical and horizontal detectors are:

$$\begin{aligned}\tilde{I}_H &= \left|E_{refH}\right|\left(\left|J_{12}+J_{11}\right|\cos(k\Delta z+\varphi_{rH}-\varphi_{x1})+\left|J_{12}-J_{11}\right|\cos(k\Delta z+\varphi_{rH}-\varphi_{x2}-\varphi)\right)\\ \tilde{I}_V &= \left|E_{refV}\right|\left(\left|J_{22}+J_{21}\right|\cos(k\Delta z+\varphi_{rV}-\varphi_{y1})+\left|J_{22}-J_{21}\right|\cos(k\Delta z+\varphi_{rV}-\varphi_{y2}-\varphi)\right)\end{aligned} \quad (2.10)$$

or

$$\begin{aligned}\tilde{I}_H &= \left|E_{refH}\right|\left(\begin{array}{l}\left|J_{12}+J_{11}\right|\cos(k\Delta z+\varphi_{rH}-\varphi_{x1})+\ldots\\ \ldots+\left|J_{12}-J_{11}\right|\left(\cos(k\Delta z+\varphi_{rH}-\varphi_{x2})\cos\varphi+\sin(k\Delta z+\varphi_{rH}-\varphi_{x2})\sin\varphi\right)\end{array}\right)\\ \tilde{I}_V &= \left|E_{refV}\right|\left(\begin{array}{l}\left|J_{22}+J_{21}\right|\cos(k\Delta z+\varphi_{rV}-\varphi_{y1})+\ldots\\ \ldots+\left|J_{22}-J_{21}\right|(\cos(k\Delta z+\varphi_{rV}-\varphi_{y2})\cos\varphi+\sin(k\Delta z+\varphi_{rV}-\varphi_{y2})\sin\varphi)\end{array}\right)\end{aligned} \quad (2.11)$$

where:

$E_{refH}=\left|E_{refH}\right|e^{i\varphi_{rH}}$, $E_{refV}=\left|E_{refV}\right|e^{i\varphi_{rV}}$,

$J_{12}+J_{11}=\left|J_{12}+J_{11}\right|e^{i\varphi_{x1}}, J_{12}-J_{11}=\left|J_{12}-J_{11}\right|e^{i\varphi_{x2}}$,

$J_{22}+J_{21}=\left|J_{22}+J_{21}\right|e^{i\varphi_{y1}}, J_{22}-J_{21}=\left|J_{22}-J_{21}\right|e^{i\varphi_{y2}}$,

k is the central wave-number and Δz is the path-length difference between the reference and sample arms (Δz = z_{ref}-z_{sample}).

Keeping in mind that the retardation φ is continuously sinusoidally modulated, i.e. $\varphi=A\sin(\omega_m t)$, we can rewrite equation 2.11 using the Bessel function expansion of sinusoidal and cosinusoidal terms in the form:

$$\sin\varphi = \sin(A\sin(\omega_m t)) = 2\sum_{j=0}^{\infty} \mathbf{J}_{2j+1}(A)\sin((2j+1)\omega_m t)$$
$$\cos\varphi = \cos(A\sin(\omega_m t)) = \mathbf{J}_0(A) + 2\sum_{j=1}^{\infty} \mathbf{J}_{2j+1}(A)\sin((2j+1)\omega_m t) \tag{2.12}$$

where $\mathbf{J_j}$ is the Bessel function of the first kind and *j*-th order. Plugging 2.12 into 2.11 and keeping only the first term in each of the sums above, we arrive at the following equations:

$$\begin{aligned}
\tilde{I}_H &= \left|E_{refH}\right|\left(\left|J_{12}+J_{11}\right|\cos(k\Delta z+\varphi_{rH}-\varphi_{x1})+\left|J_{12}-J_{11}\right|\mathbf{J}_0(A)\cos(k\Delta z+\varphi_{rH}-\varphi_{x2})\right)+\\
&+\left|E_{refH}\right|\left|J_{12}-J_{11}\right|\mathbf{J}_2(A)\left(\cos(k\Delta z+\varphi_{rH}-\varphi_{x2}+2\omega_m t)+\cos(k\Delta z+\varphi_{rH}-\varphi_{x2}-2\omega_m t)\right)+\\
&+\left|E_{refH}\right|\left|J_{12}-J_{11}\right|\mathbf{J}_1(A)\left(\cos(k\Delta z+\varphi_{rH}-\varphi_{x2}-\omega_m t)-\cos(k\Delta z+\varphi_{rH}-\varphi_{x2}+\omega_m t)\right)\\
\tilde{I}_V &= \left|E_{refV}\right|\left(\left|J_{22}+J_{21}\right|\cos(k\Delta z+\varphi_{rV}-\varphi_{y1})+\left|J_{22}-J_{21}\right|\mathbf{J}_0(A)\cos(k\Delta z+\varphi_{rV}-\varphi_{y2})\right)+\\
&+\left|E_{refV}\right|\left|J_{22}-J_{21}\right|\mathbf{J}_2(A)\left(\cos(k\Delta z+\varphi_{rV}-\varphi_{y2}+2\omega_m t)+\cos(k\Delta z+\varphi_{rV}-\varphi_{y2}-2\omega_m t)\right)+\\
&+\left|E_{refV}\right|\left|J_{22}-J_{21}\right|\mathbf{J}_1(A)\left(\cos(k\Delta z+\varphi_{rV}-\varphi_{y2}-\omega_m t)-\cos(k\Delta z+\varphi_{rV}-\varphi_{y2}+\omega_m t)\right)
\end{aligned} \tag{2.13}$$

Equations 2.13 have several terms that can be used to compute Jones matrix elements. Given the frequency band limited equipment (filters, DAQ board) it is of interest to select the components that have the lowest frequencies. Those are the terms at $k\Delta z = \omega_c t$ (carrier frequency) and at $(k\Delta z - \omega_m t) = \omega_b t$ (beating frequency). Demodulation can be done with sinusoids and cosinusoids at those frequencies. The result will be the DC terms and the double frequency terms, which can be filtered out. In the following equations symbol ⟦⟧ will denote the low-pass filtered signals.

$$H_{\sin\_\omega_b} = [\![\tilde{I}_H \sin(\omega_b t)]\!] = -\frac{1}{2}\left|E_{refH}\right|\left|J_{12} - J_{11}\right|\mathbf{J}_1(A)\sin(\varphi_{rH} - \varphi_{x2}) \tag{2.14}$$

$$H_{\cos\_\omega_b} = [\![\tilde{I}_H \cos(\omega_b t)]\!] = \frac{1}{2}\left|E_{refH}\right|\left|J_{12} - J_{11}\right|\mathbf{J}_1(A)\cos(\varphi_{rH} - \varphi_{x2}) \tag{2.15}$$

$$\begin{aligned} H_{\sin\_\omega_c} &= [\![\tilde{I}_H \sin(\omega_c t)]\!] \\ &= \frac{1}{2}\left|E_{refH}\right|\left(-\left|J_{12} + J_{11}\right|\sin(\varphi_{rH} - \varphi_{x1}) - \left|J_{12} - J_{11}\right|\mathbf{J}_0(A)\sin(\varphi_{rH} - \varphi_{x2})\right) \end{aligned} \tag{2.16}$$

$$\begin{aligned} H_{\cos\_\omega_c} &= [\![\tilde{I}_H \cos(\omega_c t)]\!] \\ &= \frac{1}{2}\left|E_{refH}\right|\left(\left|J_{12} + J_{11}\right|\cos(\varphi_{rH} - \varphi_{x1}) + \left|J_{12} - J_{11}\right|\mathbf{J}_0(A)\cos(\varphi_{rH} - \varphi_{x2})\right) \end{aligned} \tag{2.17}$$

$$V_{\sin\_\omega_b} = [\![\tilde{I}_V \sin(\omega_b t)]\!] = -\frac{1}{2}\left|E_{refV}\right|\left|J_{22} - J_{21}\right|\mathbf{J}_1(A)\sin(\varphi_{rV} - \varphi_{y2}) \tag{2.18}$$

$$V_{\cos\_\omega_b} = [\![\tilde{I}_V \cos(\omega_b t)]\!] = \frac{1}{2}\left|E_{refV}\right|\left|J_{22} - J_{21}\right|\mathbf{J}_1(A)\cos(\varphi_{rV} - \varphi_{y2}) \tag{2.19}$$

$$\begin{aligned} V_{\sin\_\omega_c} &= [\![\tilde{I}_V \sin(\omega_c t)]\!] \\ &= \frac{1}{2}\left|E_{refV}\right|\left(-\left|J_{22} + J_{21}\right|\sin(\varphi_{rV} - \varphi_{y1}) - \left|J_{22} - J_{21}\right|\mathbf{J}_0(A)\sin(\varphi_{rV} - \varphi_{y2})\right) \end{aligned} \tag{2.20}$$

$$\begin{aligned} V_{\cos\_\omega_c} &= [\![\tilde{I}_V \cos(\omega_c t)]\!] \\ &= \frac{1}{2}\left|E_{refV}\right|\left(\left|J_{22} + J_{21}\right|\cos(\varphi_{rV} - \varphi_{y1}) + \left|J_{22} - J_{21}\right|\mathbf{J}_0(A)\cos(\varphi_{rV} - \varphi_{y2})\right) \end{aligned} \tag{2.21}$$

It was shown before that the following holds true:

$$\begin{aligned} \left|E_{refH}\right| &= \left|E_{refV}\right| = \left|E_r\right| \\ \varphi_{rH} &= \varphi_r \\ \varphi_{rV} &= \varphi_r \pm \pi \end{aligned} \tag{2.22}$$

For the simplicity, we can assume that $\varphi_r = 0$ and plug the above equations into 2.14-2.21 to obtain:

$$H_{\sin\_\omega_b} = \frac{1}{2}\left|E_r\right|\left|J_{12} - J_{11}\right|\mathbf{J}_1(A)\sin(\varphi_{x2}) = \frac{1}{2}\left|E_r\right|\mathbf{J}_1(A)\left(J_{12i} - J_{11i}\right) \tag{2.23}$$

$$H_{\cos\_\omega_b} = \frac{1}{2}\left|E_r\right|\left|J_{12} - J_{11}\right|\mathbf{J}_1(A)\cos(\varphi_{x2}) = \frac{1}{2}\left|E_r\right|\mathbf{J}_1(A)\left(J_{12r} - J_{11r}\right) \tag{2.24}$$

$$\begin{aligned} H_{\sin\_\omega_c} &= \frac{1}{2}\left|E_r\right|\left(\left|J_{12} + J_{11}\right|\sin(\varphi_{x1}) + \left|J_{12} - J_{11}\right|\mathbf{J}_0(A)\sin(\varphi_{x2})\right) \\ &= \frac{1}{2}\left|E_r\right|\left((J_{12i} + J_{11i}) + \mathbf{J}_0(A)(J_{12i} - J_{11i})\right) \end{aligned} \tag{2.25}$$

$$\begin{aligned} H_{\cos\_\omega_c} &= \frac{1}{2}\left|E_r\right|\left(\left|J_{12} + J_{11}\right|\cos(\varphi_{x1}) + \left|J_{12} - J_{11}\right|\mathbf{J}_0(A)\cos(\varphi_{x2})\right) \\ &= \frac{1}{2}\left|E_r\right|\left((J_{12r} + J_{11r}) + \mathbf{J}_0(A)(J_{12r} - J_{11r})\right) \end{aligned} \tag{2.26}$$

for the horizontal channel, and:

$$V_{\sin\_\omega_b} = -\frac{1}{2}\left|E_r\right|\left|J_{22} - J_{21}\right|\mathbf{J}_1(A)\sin(\varphi_{y2}) = -\frac{1}{2}\left|E_r\right|\mathbf{J}_1(A)(J_{22i} - J_{21i}) \tag{2.27}$$

$$V_{\cos\_\omega_b} = -\frac{1}{2}\left|E_r\right|\left|J_{22} - J_{21}\right|\mathbf{J}_1(A)\cos(\varphi_{y2}) = -\frac{1}{2}\left|E_r\right|\mathbf{J}_1(A)(J_{22r} - J_{21r}) \tag{2.28}$$

$$\begin{aligned} V_{\sin\_\omega_c} &= \frac{1}{2}|E_r|\left(-|J_{22}+J_{21}|\sin(\varphi_{y1})-|J_{22}-J_{21}|\,\mathbf{J}_0(A)\sin(\varphi_{y2})\right) \\ &= -\frac{1}{2}|E_r|\left((J_{22i}+J_{21i})+\mathbf{J}_0(A)(J_{22i}-J_{21i})\right) \end{aligned} \tag{2.29}$$

$$\begin{aligned} V_{\cos\_\omega_c} &= \frac{1}{2}|E_r|\left(-|J_{22}+J_{21}|\cos(\varphi_{y1})-|J_{22}-J_{21}|\,\mathbf{J}_0(A)\cos(\varphi_{y2})\right) \\ &= -\frac{1}{2}|E_r|\left((J_{22r}+J_{21r})+\mathbf{J}_0(A)(J_{22r}-J_{21r})\right) \end{aligned} \tag{2.30}$$

for the vertical channel, where indices *i* and *r* denote imaginary and real parts of the complex variables, respectively. Equations 2.23-2.30 can be used to calculate Jones matrix elements. The final equations are:

$$\begin{aligned} J_{11r} &= \frac{H_{\cos\_\omega_c}}{|E_r|}-\frac{H_{\cos\_\omega_b}}{|E_r|\,\mathbf{J}_1(A)}\left(1+\mathbf{J}_0(A)\right) \\ J_{11i} &= \frac{H_{\sin\_\omega_c}}{|E_r|}-\frac{H_{\sin\_\omega_b}}{|E_r|\,\mathbf{J}_1(A)}\left(1+\mathbf{J}_0(A)\right) \end{aligned} \tag{2.31}$$

$$\begin{aligned} J_{12r} &= \frac{H_{\cos\_\omega_c}}{|E_r|}+\frac{H_{\cos\_\omega_b}}{|E_r|\,\mathbf{J}_1(A)}\left(1-\mathbf{J}_0(A)\right) \\ J_{12i} &= \frac{H_{\sin\_\omega_c}}{|E_r|}+\frac{H_{\sin\_\omega_b}}{|E_r|\,\mathbf{J}_1(A)}\left(1-\mathbf{J}_0(A)\right) \\ J_{21} &= J_{12} \end{aligned} \tag{2.32}$$

$$J_{22r} = -\left(\frac{V_{\cos\_\omega_c}}{|E_r|} + \frac{V_{\cos\_\omega_b}}{|E_r|\mathbf{J}_1(A)}(1-\mathbf{J}_0(A)) \right)$$
$$J_{22i} = -\left(\frac{V_{\sin\_\omega_c}}{|E_r|} + \frac{V_{\sin\_\omega_b}}{|E_r|\mathbf{J}_1(A)}(1-\mathbf{J}_0(A)) \right) \quad (2.33)$$

The above equations were derived under the condition that the phase modulation is continuous and sinusoidal. It is important that the polarization modulator is not saturated at any point – hence, the amplitude A in the above equations has to be selected accordingly. If the modulator is saturated, the phase retardation will be constant during the saturation time and the demodulation shown in equations 1.14-1.21 will not produce DC components of interest.

For the algorithm to work, it is not important how wide the range of phase modulation is as long as the modulation is constantly sinusoidal. The amplitude A will determine the range. Ideally, A can be set at 2.405 so that $\mathbf{J}_0(A = 2.405) = 0$. This amplitude depends on the physical properties of the crystal (width and length, material), wavelength, and the driving voltage waveform amplitude (linear dependency).

4. System verification

We first verified the system's performance by measuring resolution and sensitivity. The depth resolution depends on the characteristics of the light source and was measured to be 14 μm in air (10 μm in biological tissue assuming an index of refraction of 1.4). This is comparable to the theoretical value of 12.5 μm in air, which can be calculated (assuming the Gaussian power spectral density distribution of light) from

$$\Delta z = \frac{2\ln 2}{\pi}\frac{\lambda_0^2}{\Delta\lambda} \tag{2.34}$$

where λ_0 is the central wavelength of the light source and $\Delta\lambda$ is the full width at half maximum (FWHM) bandwidth of the light source power density profile. The resolution was determined by imaging the surface of a glass plate and measuring the FWHM of a representative longitudinal scan (depth scan or A-scan), as shown in Figure 2.3.

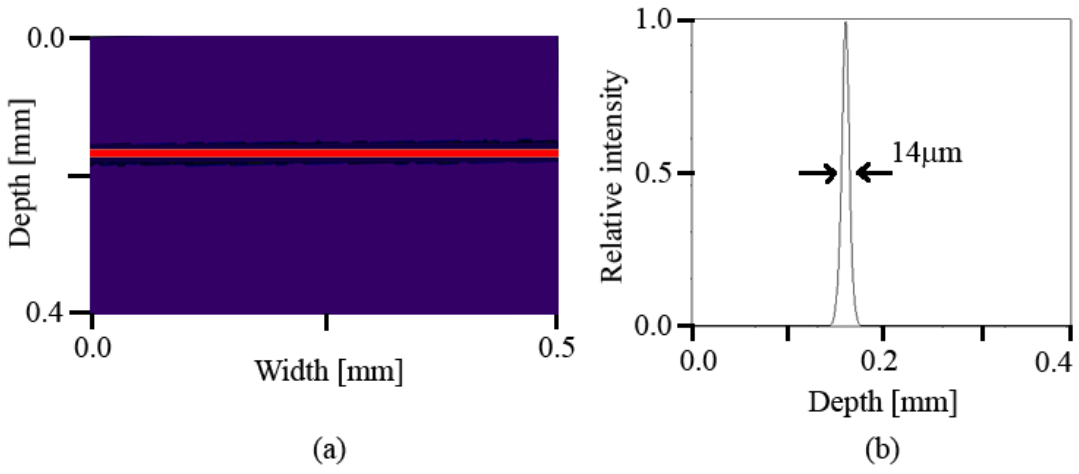

Fig. 2.3. OCT image of the flat surface of a glass plate imaged in air (a) and a typical A-scan profile extracted from the OCT image.

The sensitivity was measured by imaging a standard mirror through a set of neutral density filters of known attenuation. The number of filters in the set, and consequently

the attenuation, were increased until the mirror surface was indiscernible from noise. The sensitivity was determined to be 78 dB.

Next, the system was tested with a standard polarization element — a quarter-wave ($\lambda/4$) plate cascaded by a mirror as the sample. The fast axis of the wave plate was set at various orientations. Twenty depth scans were performed for each orientation of the $\lambda/4$ plate. The measured Jones matrix at the sample surface was used to eliminate the polarization effect of the sampling fiber [29]. The round-trip retardation and the orientation of the fast axis of the wave plate were calculated from the measured Jones matrices. The results match the expected values satisfactorily, as shown in Figure 2.4, which validates the experimental system.

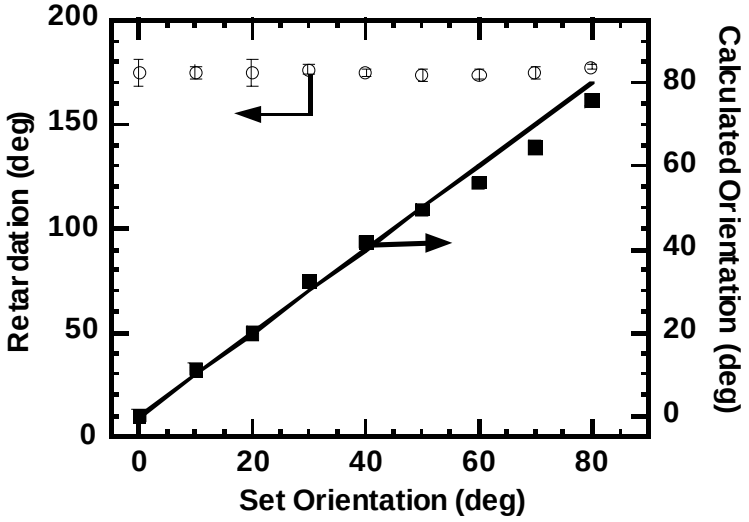

Fig. 2.4. Mean values and standard deviations of the round-trip retardation and orientation of the fast axis for a λ/4 plate calculated from the measured Jones matrix. Most of the error bars are smaller that the size of the marker.

5. Conclusions

Chapter II has presented a new high-speed, fiber-based Mueller-matrix OCT system with continuous source-polarization modulation. The system is capable of real-time imaging with a resolution of 10 μm and a sensitivity of 78 dB in biological tissue. For *in vivo* experimentation, the sample arm optics are integrated into a hand-held probe. The algorithm for the extraction of Jones matrix elements has been derived in depth and the system was characterized and verified by imaging standard optical elements, such as mirrors and quarter-wave plate.

CHAPTER III

DIFFERENTIATION ALGORITHM

1. Introduction

Polarization-sensitive optical coherence tomography has established itself as a promising noninvasive imaging modality that offers both high resolution and multiple contrast mechanisms. Birefringence contrast describes the anisotropy of the phase velocity of light in a sample which is inherent in a variety of biological components, such as collagen, myelin, and elastic fibers [7, 8, 20, 30-33]. However, the potential of birefringence contrast for determining the depth-resolved local polarization properties and the structures of samples has not been fully exploited due to the integrating nature of phase retardation along the optical path. This chapter presents a new differentiation algorithm based on the polar decomposition of Jones matrices and the subsequent least-squares regression analysis. The algorithm is capable of extracting the polarization parameters of small segments at all depths along the axial scans in the sample even in the presence of diattenuation.

Jiao *et al* have shown [30] that a scattering sample acts as a nondepolarizing medium because of the interference-based heterodyne detection scheme used in OCT. Therefore, the polarization properties of biological samples can be described equally by either Jones or Mueller matrices. The algorithm presented here is based on the Jones calculus. Following subchapters show the derivation of the differentiation algorithm followed by its application in determining localized properties of biological samples.

2. Algorithm derivation

The Jones matrix for a given depth along each A-scan obtained from Mueller-OCT encompasses the integrated effect of all of the segments within the depth:

$$J_{emi} = J_{st1}^{T} \ldots J_{st(i-1)}^{T} J_{rti} J_{st(i-1)} \ldots J_{st1}, \tag{3.1}$$

where index *emi* denotes the expected measured Jones matrix based on the signals backscattered from the *i*-th segment; *sti* represents the one-way or actual Jones matrix of the *i*-th segment; and *rti* denotes the round-trip matrix of the *i*-th segment ($J_{rti} = J_{sti}^{T} J_{sti}$). Algebraically, we can recover any round-trip single-segment matrix by recovering the one-way single-segment matrices of the preceding segments one-by-one and eliminating their integrating effects:

$$J_{rti} = (J_{st(i-1)}^{T})^{-1} \ldots (J_{st1}^{T})^{-1} J_{emi} (J_{st1})^{-1} \ldots (J_{st(i-1)})^{-1}. \tag{3.2}$$

We need to assume a model of a tissue segment to proceed with characterizing its properties. A sequence of a linear diattenuator and a linear retarder can model a thin segment of biological tissue well. This model is reasonable because physical properties, such as the orientation of the collagen fibers, are almost constant at the scale of OCT resolution (~10 μm). It is further assumed that the orientations of the retarder and diattenuator are the same, which is logical since their orientations are directly related to

the orientation of the tissue fibers. In this case, the order between the diattenuator and retarder is irrelevant and the thin tissue segment is referred to as homogeneous in the sense of polarimetry. The equivalent one-way Jones matrix of a segment is given by

$$J_{st} = \begin{bmatrix} Q_x \cos^2\theta + Q_y \sin^2\theta & (Q_x - Q_y)\sin\theta\cos\theta \\ (Q_x - Q_y)\sin\theta\cos\theta & Q_x \sin^2\theta + Q_y \cos^2\theta \end{bmatrix},$$
$$Qx = p_x \exp\left(\frac{i\varphi}{2}\right), \tag{3.3}$$
$$Qy = p_y \exp\left(-\frac{i\varphi}{2}\right),$$

where φ is the phase retardation; θ is the orientation angle of the fast eigenvector for both the diattenuator and retarder; and p_x and p_y are the transmittances of the fast and slow eigenvectors, respectively. The round-trip single-segment Jones matrix closely resembles the one-way matrix except that the transmittances are $p_x' = p_x^2$ and $p_y' = p_y^2$, and the retardation is doubled to $\varphi' = 2\varphi$. The orientation retains its original value θ. Therefore, it is not necessary to obtain the one-way matrix in order to calculate the values of φ, θ, p_x, and p_y as the round-trip matrix will suffice.

The polar decomposition theorem, when used with Jones matrices, states that any non-depolarizing polarization element described by a Jones matrix can be represented as a cascade of a diattenuator and a retarder [27]. The polar decomposition yields two matrices – a unitary matrix U corresponding to a retarder and a nonnegative definite Hermitian matrix H corresponding to a diattenuator. Once the round-trip matrices of the

individual segments are calculated, we can apply the polar decomposition to obtain matrices U and H. To calculate the parameters of an individual segment, we fit the matrices U and H to the model Jones matrices of a linear retarder and linear diattenuator in the least–squares sense, respectively.

Knowing the Jones matrices for the retarder ($\varphi' = 2\varphi$, θ) and diattenuator ($p_x' = p_x^2$, $p_y' = p_y^2$, θ) and having the decomposed measured round-trip matrix of the individual segment in the form $J_m = U_m H_m$, one can apply the least-squares method that minimizes the difference between the measured and expected Jones matrices to calculate the parameters of interest. Sums S_1 and S_2 shown below are the base equations of the least-squares algorithm for calculating the parameters of the equivalent retarder and diattenuator, respectively:

$$S_1 = \sum_{i=1,j=1}^{2,2} (U_{m\,i,j} - J_{retarder\,i,j})^2$$
$$S_2 = \sum_{i=1,j=1}^{2,2} (H_{m\,i,j} - J_{diattenuator\,i,j})^2. \qquad (3.4)$$

Minimization of S_1 with respect to θ and φ and S_2 with respect to p_x and p_y yields expressions for calculating the orientation, retardation, and transmission parameters as shown below:

$$\tan 2\theta = \frac{U^i_{m12} + U^i_{m21}}{U^i_{m11} - U^i_{m22}},$$

$$\cot \varphi = \frac{U^r_{m11} + U^r_{m22}}{(U^i_{m11} - U^i_{m22})\cos 2\theta + (U^i_{m12} + U^i_{m21})\sin 2\theta}, \tag{3.5}$$

$$p_x = [H^r_{m11}\cos^2\theta + H^r_{m22}\sin^2\theta + (H^r_{m12} + H^r_{m21})\sin\theta\cos\theta]^{1/2},$$

$$p_y = [H^r_{m11}\sin^2\theta + H^r_{m22}\cos^2\theta - (H^r_{m12} + H^r_{m21})\sin\theta\cos\theta]^{1/2}.$$

Given the amplitude transmittances p_x and p_y, we can calculate the diattenuation for each segment as $D = |p_x^2 - p_y^2|/(p_x^2 + p_y^2)$. Because $p_{x,y}$ and D are integrated parameters over the finite pathlength, we define the dual attenuation coefficients μ_{ax} and μ_{ay} as fractions of the intensity attenuation per unit infinitesimal length along the fast and slow axes, respectively, each having an unit of inverse length and being independent of the finite pathlength. In case of homogeneous properties along an A-scan, we can extend the Beer's law to $p_{x,y}^2 = \exp(-\mu_{ax,y}t)$, where t is the thickness of the sample. We can also calculate diattenuation as $D = \tanh(|\mu_{ax} - \mu_{ay}|t/2)$.

3. Results and discussion

The differentiation algorithm was applied to calculate polarization parameters of biological samples including a section of homogeneous porcine tendon and a piece of heterogeneous septum from a rat heart. The Jones matrices were measured using the Mueller-OCT system with the dynamic calibration technique for eliminating the effects

of birefringence of the single-mode fiber [29]. To convert from optical pathlength to physical depth, we assumed the index of refraction to be 1.4.

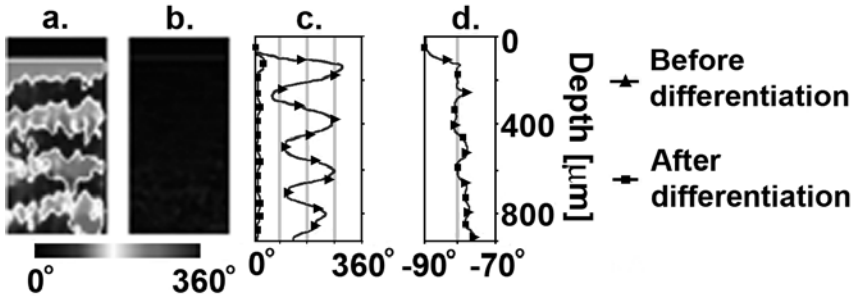

Fig. 3.1. Retardation images of porcine tendon before differentiation (a) and after differentiation (b); profiles of averaged phase retardation before and after differentiation (c); and profiles of averaged slow-axis orientation before and after differentiation (d). Dimensions of each OCT image are 0.5mm × 0.9mm (width × height).

Figure 3.1 shows the phase retardation images prior to the differentiation (a) and after the differentiation algorithm (b) was applied, as well as the profiles of the corresponding retardation (c) and slow axis orientation (d) averaged across all 50 A-scans. The periodical structure in the retardation image in Figure 3.1(a), resulting from the 360 degrees phase wrapping, is a manifestation of the integrating nature of phase retardation. Previously published images of porcine tendon showed 180 degrees phase wrapping patterns; inspection of the fast-axis orientation revealed an abrupt 90-degree shift at each point of phase wrapping. This is consistent with the fact that a retarder $J(\varphi =$

$\pi + \delta, \theta)$ is equivalent to a retarder $J(\varphi = \pi - \delta, \theta + \pi/2)$; hence, a phase wrapping of 180 degrees induces an orientation shift of 90 degrees. The extension of the phase retardation range to 360 degrees in this study was achieved by keeping the depth profile of the orientation smooth. As a result, the differentiated retardation image shown in Figure 3.1(b) is nearly uniform. The differentiated phase retardation of ~15 degrees per 10 μm segment length (birefringence: 3.5×10^{-3}) is comparable with previously reported values [8, 20] and shows no periodical structures any more. The slow-axis orientation is nearly constant and corresponds to the orientation of the type I collagen fibers in tendons. This allowed us to calculate attenuation coefficients for porcine tendon (95% confidence interval): $\mu_{ax} = 0.19 \pm 0.02$ mm^{-1}, $\mu_{ay} = 0.29 \pm 0.02$ mm^{-1}, and the corresponding round-trip diattenuation D is 0.10 ± 0.02 for the 1 mm thick tendon sample. Note that the higher attenuation is along the collagen fibers (the slow axis).

Finally, we investigated the phase retardation and changing orientation of muscle fibers in the septum of a rat heart. The heart tissue was fixed in 10% buffered neutral formalin before imaging. Upon completion of the OCT imaging, the paraffin-embedded tissue was sectioned into 20 μm thick layers and stained with hematoxylin and eosin (HE). The stained sections were examined under an Olympus light microscope with 40× magnification to quantify the orientation of muscle fibers at various depths, where all of the angles were measured with respect to the horizontal polarization axis. Figure 3.2 presents the results of the analysis of the septum from the surface up to a depth of 680 μm along one A-scan. In order to improve the SNR, the A-scan used to calculate the orientation and phase retardation is a result of averaging 50 measurements at the same

location. Slow-axis orientation values obtained using the differentiation algorithm are in good agreement with the data from the histology. As expected, the standard deviation increases with depth due to the decreasing SNR. The muscle-fiber orientation values increase almost linearly from the surface up to the 360 μm where there is a negative change after which we again observe a linear increase. The discontinuity in the positive slope of the fiber orientation change may be the result of a trabeculata-compacta interface [34] in the region of the septum proximal to the ventricular wall where the measurement was taken. The linear change of orientation observed in our study agrees with the results of a study [34] where the author observed that the fiber orientation linearly changes from the surface of the septum towards the deeper regions.

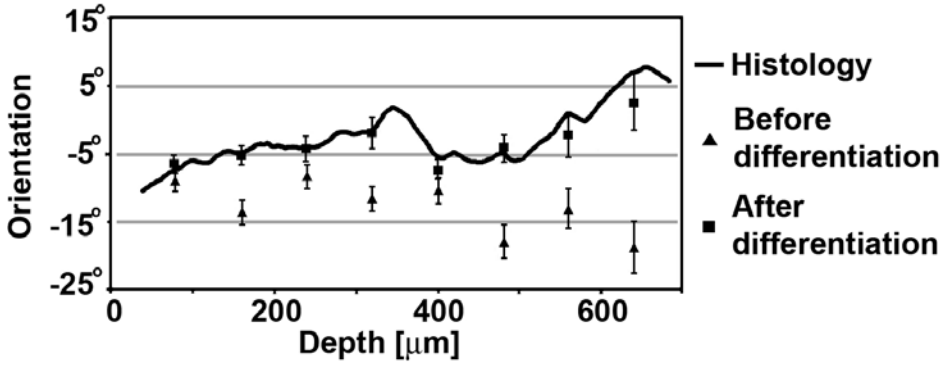

Fig. 3.2. Profiles of muscle-fiber orientation along one A-scan obtained from histological images, from Mueller-OCT after differentiation and before differentiation.

To emphasize the importance of the depth-wise differentiation, we show the orientation calculated without differentiation from the same data set. It is obvious that the orientation calculated in this way does not reflect the actual orientation as the values do not follow the profile obtained from the histology. Phase retardation in the sample is constant with depth and its values fall almost perfectly in a straight line with an average value of 0.84 ± 0.02 degrees per 10 μm segment (95% confidence interval) corresponding to a birefringence of $(1.94 \pm 0.05) \times 10^{-4}$.

4. Conclusions

In summary, this chapter introduced a novel algorithm that uses polar decomposition and least-squares fitting to recover one-way Jones matrices of individual segments within scattering media. The algorithm was successfully applied to recovering the local polarization parameters of biological samples such as the orientation of the collagen and muscle fibers and the diattenuation of the tendon. Future work will include the implementation of a speckle-reduction algorithm that should aid the differentiation by increasing the SNR. This algorithm opens a new window of opportunity for OCT imaging applications.

CHAPTER IV

BURN IMAGING

1. Introduction

The National Health Interview Survey (NHIS) estimates that there are more than 1.1 million burn injuries per year in the United States [35]. Approximately 45,000 of these injuries require hospitalization, and roughly 4,500 people die from burn injuries annually. In addition, up to 10,000 people in the United States die every year from burn-related infections.

A burn is defined as tissue damage caused by a variety of agents, such as heat, chemicals, electricity, sunlight, or nuclear radiation. The clinical significance of a burn depends on, among other things, its depth [36]. In superficial burns, the dermis is spared and often the epidermis, though devitalized, still exists. Superficial partial-thickness burns extend through the epidermis into the papillary layer of the dermis. Deep partial-thickness burns affect the reticular layer of the dermis. Finally, full-thickness burns extend through the epidermis and dermis into the subcutaneous tissue layer [37].

Without a biopsy, it is difficult to determine the depth of a burn. Currently such determinations are generally made by professionals who must make an educated guess after observing the injury for several days. A non-invasive imaging modality for evaluating burn depth would be of great help to physicians and patients. One such potential technique is polarization-sensitive optical coherence tomography (PS-OCT) [7, 8], which uses changes in the polarization properties of thermally damaged tissue to

assess the extent of a burn injury. Chapter IV demonstrates the applicability of the system for burn depth determination by imaging porcine skin *in vivo*.

2. Animal studies

All experimental procedures on the pigs were approved by the University Laboratory Animal Care Committee (ULACC) of Texas A&M University and followed the guidelines of the United States National Institutes of Health [38].

The application of the system for *in vivo* burn depth determination was first investigated by imaging porcine (Yorkshire cross, 10 kg body weight) ear skin exposed for 10 seconds to a cauter heated to 150^{o}C. The entire procedure was performed under anesthesia (preanesthetic xylazine 2.2 mg/kg, IM and anesthetic ketamine 40 mg/kg, IM). According to the ULACC approved protocol, the induced burns were treated with topical antibiotic (5%) ointment to protect wounds against bacterial contamination. Upon completion of the OCT imaging, the animal was euthanized with a pentobarbital overdose (100 mg/kg, IM). The excised skin tissue was fixed in a 10% buffered neutral formalin, and the paraffin-embedded tissue was sectioned and stained with hematoxylin and eosin (HE). The stained sections were examined under an Olympus BH-2 light microscope with 4X magnification to evaluate the thermally induced changes.

Following the successful *in vivo* imaging of the porcine ear skin, a time point experiment was performed to investigate the changes of polarization properties of porcine skin from a dorso-lateral site as the skin was healing after a burn injury. Four identical sets of burn injuries, with each set consisting of four burns, were inflicted on

the skin. Each set had burns made with the electrical cauter heated to 125^{o}C and 150^{o}C, and exposed for 10 and 30 seconds at each temperature. Again, the entire procedure was performed under anesthesia and the induced burns were treated with topical antibiotic ointment to protect wounds against bacterial contamination. The healing progress was observed bi-weekly following the injury. Upon completion of the OCT imaging at each time point, a biopsy was performed to harvest the samples for histology. At the end of the eight week period the animal was euthanized.

3. Results and discussion

The application of the system for *in vivo* burn depth determination was first investigated by imaging burnt porcine ear skin. Figure 4.1 shows the OCT intensity (a), integrated (b) and differentiated [9] (c) phase retardation images of the ear skin after burning. The HE stained histology image (d) is included for comparison.

The healthy region of the epidermis, as determined from the differentiated phase retardation image (Figure 4.1(c)), has an average birefringence of $(3.0 \pm 0.2) \times 10^{-4}$ and the healthy dermis exhibits a birefringence of $(5.1 \pm 0.2) \times 10^{-3}$ (95% confidence intervals). The loss of birefringence is visible in the thermally damaged region in Figures 4.1(b) and 4.1(c) and can be attributed to the denaturation of collagen-based connective tissue in the dermis. The marked burn areas in the phase retardation images and histology compare well with each other in shape and location.

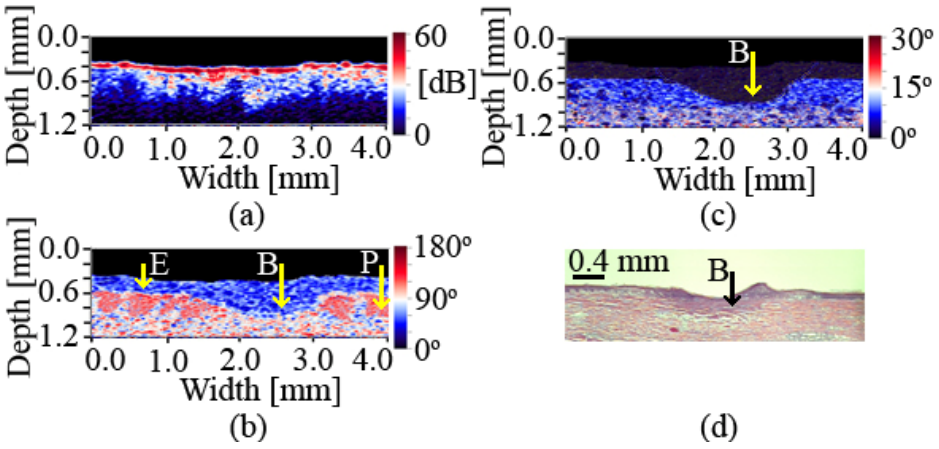

Fig. 4.1. Intensity (a), integrated (b) and differentiated (c) phase retardation, and HE stained histology (d) images of a burnt porcine ear skin. E – epidermis; P – papillae; B – burn. The burn depth is determined to be 0.47 mm (OCT) and 0.41 mm (histology). The difference in burn depth can be attributed to tissue shrinkage due to formalin fixation.

The depth of the burn determined by the OCT system is 0.47 mm, while the depth obtained from the histology is 0.41 mm. This difference in absolute depths can be attributed to tissue shrinkage due to formalin fixation and the fact that the histology cut was performed at a position that might have been slightly different from the one imaged with the OCT system. The birefringence in the burnt area is $(2.2 \pm 0.2) \times 10^{-4}$ (95% confidence interval). This value is an order of magnitude smaller than the value observed in healthy dermis and is close to the value detected in healthy epidermis. Based on the depth, the burn can be classified as a superficial partial-thickness burn according to the nomenclature presented in literature [37].

A time point experiment was designed to investigate the changes that occur in skin during the post-burn healing. Figure 4.2 shows two sets of experimental results for burns inflicted for 30 seconds at 125^{o}C. The results obtained for burns inflicted at other exposure-time/temperature combinations are similar. The upper row (Figures 4.2(a)-4.2(c)) shows the intensity, phase retardation and HE stained histology images, respectively, of the porcine skin from the dorso-lateral region immediately after burning. Second and third rows (Figures 4.2(d)-4.2(h)) show images from a second burn from the same region (identical exposure time/temperature combination) taken immediately post-burning and after 4 weeks of healing. The location of the burn is clearly identifiable in all phase retardation images. The healing process was completely natural and was not promoted by any ointments. A topical antibiotic was applied to prevent infection.

Comparison of the phase retardation images post-burn and after four weeks of healing shows marked difference in the burnt area. While the damage to the epidermis and dermis is clearly visible in the fresh burn, the epidermis and the proximal layers of dermis are almost completely healed after four weeks. However, the deeper regions of dermis are still damaged. This is consistent with the nature of the skin regeneration process where the remaining epidermis surrounding the burn will start to proliferate into the burnt region and the epidermis will close within approximately a week [39]. On the other hand, collagen fibers in dermis need more time to mature and regain their original matrix organization. The proximal dermis is pulled in towards the center of the wound by the proliferating epidermis and regenerates faster than the distal regions. The

structures observed in OCT images correspond well to the structures seen in histological analysis.

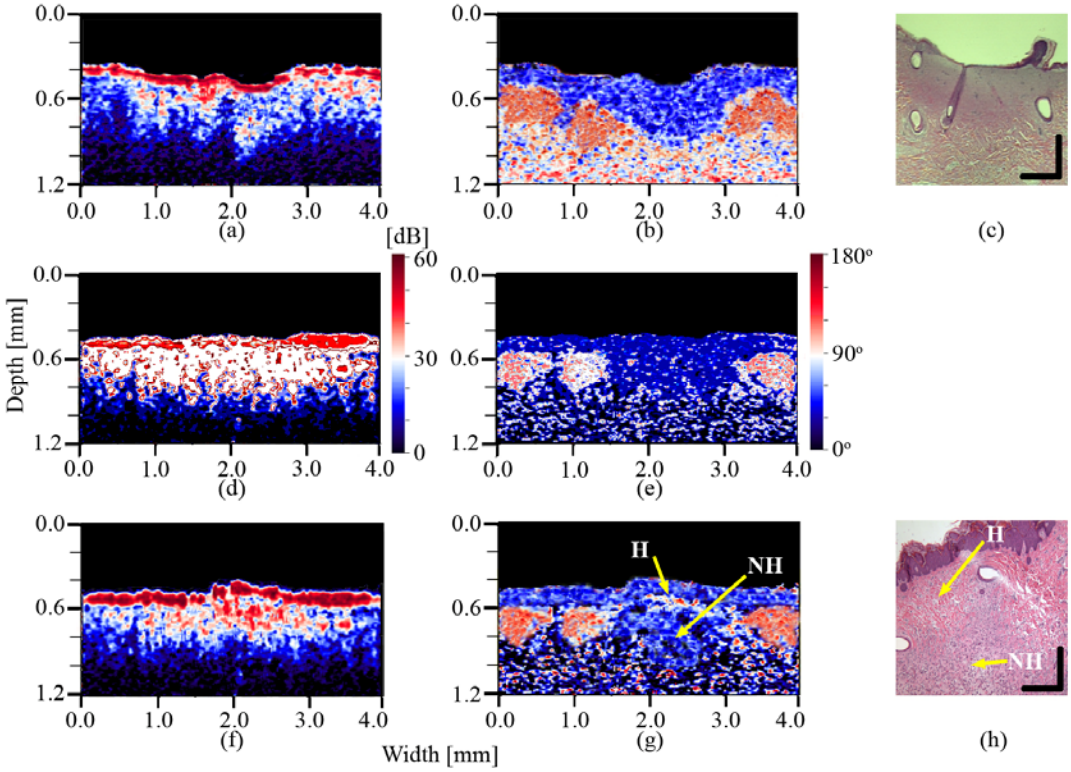

Fig. 4.2. Intensity (a), phase retardation (b) and HE stained histology (c) images of the burnt porcine dorso-lateral skin immediately following the injury; intensity (d) and phase retardation (e) images of the second burn from the same region immediately post-burning; and the intensity (f), phase retardation (g) and the and HE stained histology (h) images of the second burn after four weeks of healing. H – epidermal and proximal dermal region healed after four weeks; NH – deeper dermal region not healed after four weeks. Vertical and horizontal bars in HE stained histology images represent 0.2 mm.

4. Conclusions

In conclusion, we have presented the use of a new high-speed, fiber-based Mueller-matrix OCT system with continuous source-polarization modulation for *in vivo* burn imaging. For the first time to our knowledge, a map of the local birefringence of intravital porcine skin was presented. The system is capable of accurately localizing changes in polarization properties that are due to thermal damage of tissue *in vivo* and, hence, has the potential to aid physicians in determining the extent of burn injuries and subsequent monitoring of the skin regeneration.

CHAPTER V

EARLY CANCER DETECTION

1. Introduction

Skin cancers are the most common types of cancers occurring in humans. The National Cancer Institute of the U.S. National Institutes of Health estimates that there will be more than one million new cases of skin cancer diagnosed in 2008 in the United States alone [40]. The deadliest type of skin cancer is melanoma and it forms in melanocytes. Basal cell carcinoma (BCC) develops in the basal layer of the skin, while the skin cancer that forms in squamous cells on the surface of the skin is called squamous cell carcinoma (SCC). Finally, skin cancer that develops in neuroendocrine cells of the skin is called neuroendocrine carcinoma.

Although the overall mortality rate for all skin cancers is lower than for some other types of cancers (breast, colon, prostate, etc.), the high incidence rate has spurred a lot of interest in research of the mechanisms for early detection and treatment. Standard clinical diagnosis of skin cancer relies almost exclusively on the visual examination of tissue followed by pathological determinations of tissue biopsies collected from suspected lesions. The search for a less invasive method for rapid screening of epithelial tissue and early detection of malignant tissue transformations has significant appeal. Ideally, a method that maintains existing visualization approach by non-invasively assessing the tissue could prove to be an extremely powerful technique for early detection of epithelial hyperplasia.

Several studies have tackled non-invasive early cancer detection. Prevalent commercially available technologies, such as magnetic resonance imaging [41] and ultrasound [42], suffer from low resolution and have not proven to be good candidates for early detection of superficial tumors. Stepinac *et al* have investigated the intraepithelial neoplasiae in Barrett's esophagus using endoscopic fluorescence imaging [43]. The ability of fluorescence imaging to detect the formation of hyperplasiae and neoplasiae on a macroscopic scale has been used to guide optical coherence tomography in examination of bladder [44] and oral cavity [45] cancers on a microscopic scale. It has been shown that OCT is capable of detecting precancerous lesions with far better accuracy than fluorescence due to the superior resolution. Garcia-Uribe *et al* have used spectroscopic oblique-incidence reflectometry to classify skin lesions [46]. Their pilot study achieved a high accuracy in detecting BCC and SCC lesions but their system does not provide visualization of the lesion. Evaluation of superficial pigmented lesions by reflectance-mode confocal microscopy and OCT has been carried out by Yamashita *et al* [47]. Strasswimmer *et al* have used polarization-sensitive optical coherence tomography (PS-OCT) to investigate the fully developed invasive BCC [48]. They have shown that the PS-OCT is capable of delineating the cancer borders using the polarization contrast, which can help guide surgeons in the treatment of aggressive skin cancer.

The applicability of the Mueller OCT system for early skin cancer detection is demonstrated here by imaging SENCAR mice skin *in vivo*.

2. Animal studies

The applicability of the Mueller OCT to skin cancer imaging was tested using a well-established model of 7, 12-dimethylbenz(a)anthracene (DMBA)-induced squamous cell carcinoma in SENCAR mice [49]. The SENCAR stock of mice was selectively bred for sensitivity to skin tumor induction by two-stage tumorigenesis using DMBA as the tumor initiator and 12-O-tetradecanoylphorbol-13-acetate (TPA) as the promoter. In this study, 30 female SENCAR mice, 7-8 weeks old, were randomly divided into three groups of 10. Each animal was shaved on the dorsal side of the skin. All chemicals were applied topically with a cotton swab. The first group was treated with 0.2 ml of acetone. Second group of mice was treated with TPA (0.2 ml of acetone containing 2 micrograms of TPA) only. The third group was first treated with DMBA (10 nmol dose dissolved in 0.2 ml of acetone per mouse) once to initiate the tumorigenesis and then, starting one week after initiation, treated with TPA (0.2 ml of acetone containing 2 micrograms of TPA). The TPA and acetone treatments were repeated once per week up to the termination of the experiment at the 20^{th} week. Groups I and II served as controls. OCT imaging was performed bi-weekly on one randomly selected animal from each group. Immediately following imaging, the animals were euthanized using the CO_2 method. The excised skin tissue was fixed in a 10% buffered neutral formalin, and the paraffin-embedded tissue was sectioned and stained with hematoxylin and eosin (HE). In addition, the unstained samples were preserved for examination with cross-polarized light microscopy for birefringence detection. The histology slides were examined under an Olympus BH-2 light microscope. All experimental procedures on SENCAR mice

were approved by the University Laboratory Animal Care Committee (ULACC) of Texas A&M University and followed the guidelines of the United States National Institutes of Health [38].

3. Results and discussion

The applicability of the Mueller OCT system for skin cancer detection was tested by imaging dorsal skin of SENCAR mice from all three groups *in vivo*. The experimental results showed no significant difference in skin morphology between the mice in two control groups (groups I and II). OCT images presented here were acquired 12 weeks after DMBA initiation.

Figure 5.1 presents OCT images from a set of 5 measurements taken in succession at the same location on the back of a healthy SENCAR mouse. The purpose of this test is to prove the repeatability of measurements, which is important in this study due to the fact that each animal was imaged only at one time point and immediately sacrificed following imaging.

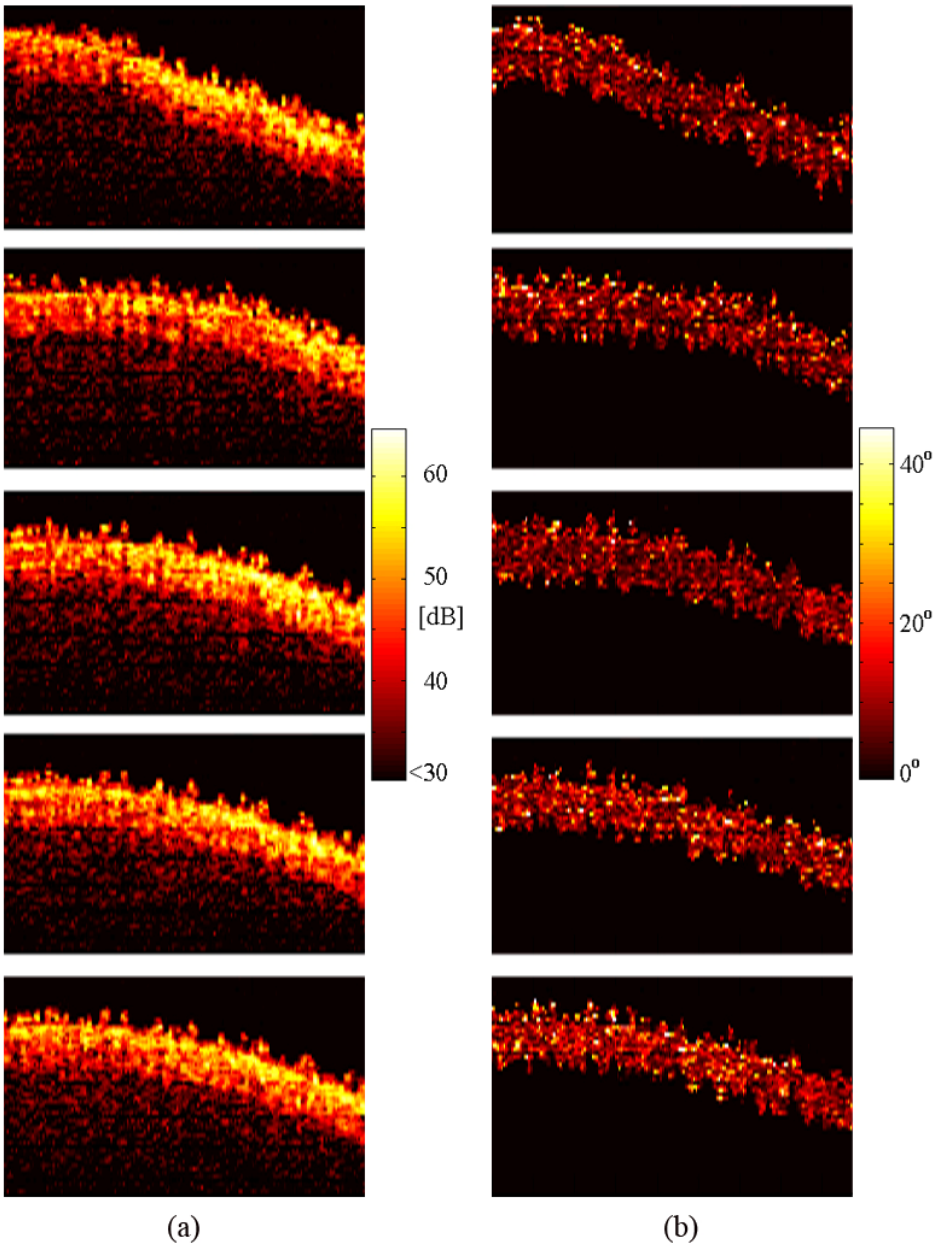

Fig. 5.1. Intensity (a) and phase retardation (b) images of healthy SENCAR mouse dorsal skin. A set of 5 OCT *in vivo* measurements at the same location proves the repeatability of measurements. Each OCT image is 2 mm wide and 1.2 mm deep.

Correlation matrices for the intensity and phase retardation images are

$$r_{\text{intensity}} = \begin{bmatrix} 1.0 & 0.472 & 0.6143 & 0.6175 & 0.6188 \\ & 1.0 & 0.6787 & 0.6027 & 0.597 \\ & & 1.0 & 0.7954 & 0.7939 \\ & & & 1.0 & 0.8724 \\ & & & & 1.0 \end{bmatrix} \tag{5.1}$$

$$r_{\text{phase retardation}} = \begin{bmatrix} 1.0 & 0.354 & 0.3298 & 0.3425 & 0.3612 \\ & 1.0 & 0.4088 & 0.3573 & 0.3458 \\ & & 1.0 & 0.5046 & 0.4991 \\ & & & 1.0 & 0.6119 \\ & & & & 1.0 \end{bmatrix} \tag{5.2}$$

where $r_{i,j}$ are the correlation coefficients between i-th and j-th images in the set. Correlation coefficients were calculated after the images were thresholded to minimize the influence of noise outside the areas of interest. Each correlation coefficient was tested for significance using Student's t-test with the significance level $\alpha=0.05$ [50]. Tests showed that the null hypothesis (no correlation) can be rejected in all cases. The difference from the ideal correlation levels can likely be attributed to motion artifacts.

Figure 5.2 shows intensity (a), HE stained histology (b), phase retardation (c), and cross-polarized unstained histology (d) images of healthy SENCAR mouse dorsal skin from group I. Typically, the thickness of the cutis (epidermis and dermis) in healthy mice is in the range of 250-400 μm. In the OCT images in Figure 5.2 there is a visible boundary between the dermis and subcutaneous tissue at the depth of approximately 300

μm, which is in agreement with histology. Subcutis is mainly composed of adipose tissue whose backscattered reflectance is low [51], which explains the low intensity of backreflected light originating from this region.

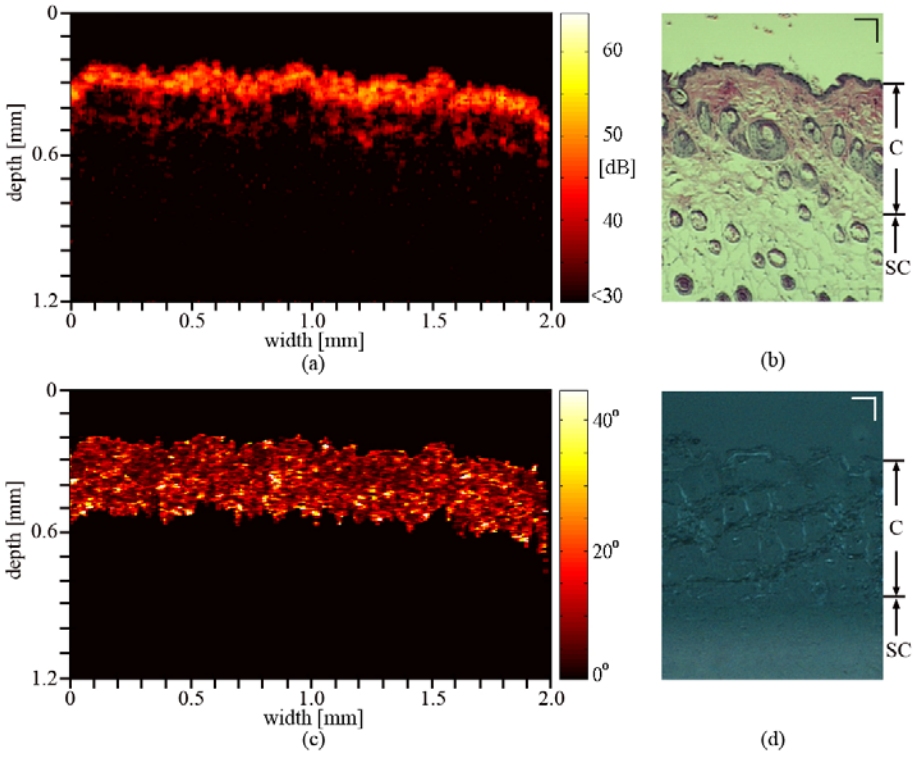

Fig. 5.2. Intensity (a), HE stained histology (b), phase retardation (c), and cross-polarized unstained histology (d) images of healthy SENCAR mouse dorsal skin. C, cutis; SC, subcutaneous tissue. Bars in histology images represent 100 μm.

The phase retardation image reveals a low magnitude retardation (up to 50 degrees) indicating weaker birefringence in SENCAR mice skin. The phase retardation is

confined within the dermal region, which is consistent with the presence of collagen fibers whose structural organization gives rise to birefringence. In alignment with phase retardation image, cross-polarized histology image also reveals weak birefringence.

Figure 5.3 presents the intensity (a), HE stained histology (b), phase retardation (c), and cross-polarized unstained histology (d) images of SENCAR mouse dorsal skin with pre-cancerous papilloma formations.

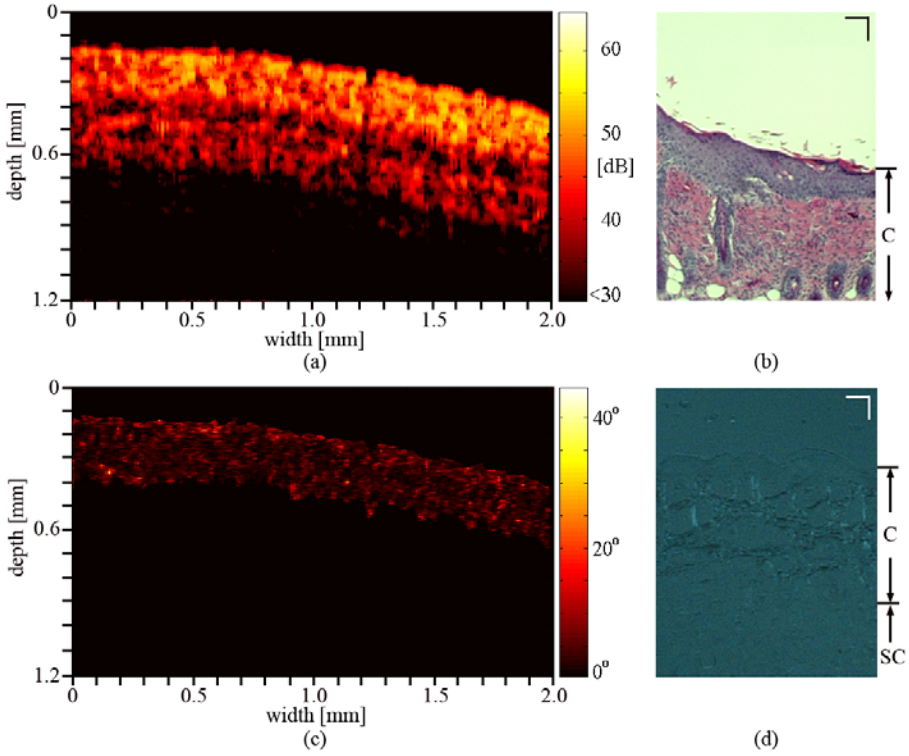

Fig. 5.3. Intensity (a), HE stained histology (b), phase retardation (c), and cross-polarized unstained histology (d) images of SENCAR mouse dorsal skin with pre-cancerous papilloma formations. C, cutis; SC, subcutaneous tissue. Bars in histology images represent 100 μm.

Intensity image shows the wider cutis (500 μm) due to the proliferation of epidermis and dermis (hyperplasia), which is a typical process in early phases of tumorigenesis. Another important finding is the significant reduction in phase retardation (less than half of that in unaffected skin). The sustained cellular hyperplasia plays a critical role in tumor promotion [52] and is the first indication of potential cancerous formation. The ability to observe these early changes in skin anatomy is important for early cancer detection. The rapid growth of dermis is promoted by the creation of new collagen fibers. These new fibers are immature and not well organized, which reduces the overall birefringence as indicated in the phase retardation image and cross-polarized histology in Figures 5.3(c) and 5.3(d), respectively. The observed reduction in birefringence in the affected region is consistent with the previously published results in case of invasive BCC [48].

4. Conclusions

In conclusion, we have presented the use of a high-speed, fiber-based Mueller-matrix OCT system with continuous source-polarization modulation for *in vivo* imaging of skin cancer in a SENCAR mouse model. The system is capable of detecting changes in skin brought about by proliferation of epidermal and dermal tissue as a response to tumor initiation and promotion. The increased depth of cutis coupled with the loss of birefringence, both of which are observed in PS-OCT images, is an indicator of pre-cancerous hyperplasia leading to the cancerous SCC.

CHAPTER VI

CONCLUSIONS

1. Summary

Optical imaging of soft biological tissue is highly desirable due to its non-ionizing nature, excellent resolution, and its ability to provide sensitive contrast information which enables, among other things, potential early cancer detection and burn injury assessment. To stress the importance of the need for optical imaging note that the current techniques for, for example, cancer detection (ultrasound, x-ray computerized tomography, and magnetic resonance imaging) are not very efficient in detecting lesions smaller than ~1 cm. As a result, most of the cancers detected by these methods are in advanced stages, and development of new techniques for early cancer detection is an imperative.

One of the optical imaging modalities allowing for high resolution imaging is the optical coherence tomography. As an extension of previous work, a new high-speed, fiber-based Mueller-matrix OCT system with continuous source-polarization modulation was developed and presented in Chapter II. The system is capable of real-time imaging with a resolution of 10 μm and a sensitivity of 78 dB in biological tissue. For *in vivo* experimentation, the sample arm optics are integrated into a hand-held probe. The algorithm for the extraction of Jones matrix elements has been derived in depth and the system was characterized and verified by imaging standard optical elements, such as mirrors and quarter-wave plate.

The optical properties of soft biological tissues in the visible and near-infrared regions of the optical spectrum are related to the molecular and cellular structure, offering potential for the investigation of tissue morphology (optical biopsy), physiology and pathology. For example, cancer-related tissue abnormalities, such as angiogenesis, hyper-metabolism, and invasion into adjacent normal tissue, possess optical signatures (polarization, scattering and absorption) that offer the potential for early cancer detection. A key polarization parameter is birefringence, which describes the anisotropy of the phase velocity of light in a sample and is inherent in a variety of biological components, such as collagen, myelin, and elastic fibers. However, the potential of birefringence contrast for determining the depth-resolved local polarization properties and the structures of samples has not been fully exploited due to the integrating nature of phase retardation along the optical path.

Chapter III introduced a novel algorithm that uses polar decomposition and least-squares fitting to recover one-way Jones matrices of individual segments within scattering media. The algorithm was experimentally verified using measurements of a section of porcine tendon and the septum of a rat heart. It was successfully applied to recovering the local polarization parameters of biological samples such as the orientation of the collagen and muscle fibers and the diattenuation of the tendon. In addition, a new concept of dual attenuation coefficients to characterize diattenuation per unit infinitesimal length in tissues was introduced. This algorithm opens a new window of opportunity for OCT imaging applications, such as non-contact optical biopsy.

Following the successful development of the system and differentiation algorithm, the system was used for two extensive animal studies. The first application was the *in vivo* burn imaging and subsequent wound healing monitoring. For the first time to our knowledge, a map of the local birefringence of *intravital* porcine skin was presented. It was shown that the system is capable of accurately localizing changes in polarization properties that are due to thermal damage of tissue *in vivo* and, hence, has the potential to aid physicians in determining the extent of burn injuries and subsequent monitoring of the skin regeneration.

Another major study was the *in vivo* imaging of skin cancer on the SENCAR mice model. The results confirmed that the system is capable of detecting changes in skin morphology brought about by proliferation of epidermal and dermal tissue as a response to tumor initiation and promotion. The increased depth of cutis coupled with the loss of birefringence, both of which were observed in PS-OCT images, is an indicator of pre-cancerous hyperplasia leading to the cancerous squamous cell carcinoma. The ability of the system to detect these early non-cancerous stages of the tumorigenesis suggests the potential value of the system for preventive screening for skin cancers.

2. Other applications

In addition to the work presented here, the Mueller PS-OCT system was used for the evaluation of the magneto-optical effect in biological tissue models using optical coherence tomography [53]. For the first time, an experimental evaluation of the Faraday effect–induced polarization rotation in a biological tissue phantom was reported in this

study. The rotation of the polarization plane produced in the optical beam propagating through an Intralipid solution was evaluated using polarization-sensitive optical coherence tomography, and the experimental results closely matched the theoretical values. It was shown that the angle of rotation is proportional to the traversed path length along the magnetic field and can potentially be used to estimate the actual penetration depth.

3. Future work

Biopsy and histologic processing remain the gold standard for tissue disease and abnormalities diagnosis. With the improvements in the depth resolution and sensitivity, and the inclusion of polarization sensitive contrasts, optical coherence tomography has a potential to approach the level of detail offered by histologic processing while preserving the integrity of the specimen due to OCT's non-invasive imaging. A logical extension of the work presented in this dissertation is the development of the new polarization-sensitive system using ultra-broadband light sources, which can bring the depth resolution of the system to the sub-micrometer levels. Application of the new system in dermatology would yield enhanced level of detail and potentially show new parameters that could be used by physicians in diagnostics of cancers and the extent of burn damage.

REFERENCES

1. L.V. Wang, "Ultrasound-mediated biophotonic imaging: A review of acousto-optical tomography and photo-acoustic tomography," Dis. Markers **19**, pp. 123-138 (2004).

2. S. Jiao, W. Yu, G. Stoica, and L.V. Wang, "Contrast mechanisms in polarization-sensitive Mueller-matrix optical coherence tomography and application in burn imaging," Appl. Opt. **42**, 5191-5197 (2003).

3. S.M. Srinivas, J.F. de Boer, H.P.K. Keikhanzadeh, H.L. Huang, J. Zhang, W.Q. Jung, Z. Chen, and J.S. Nelson, "Determination of burn depth by polarization-sensitive optical coherence tomography," J. Biomed. Opt. **9**, 207-212 (2004).

4. P.T.C. So, C.Y. Dong, B.R. Masters, and K.M. Berland, "Two-photon excitation fluorescence microscopy," Annu. Rev. Biomed. Eng. **2**, 399-429 (2000).

5. D. Huang, E.A. Swanson, C.P. Lin, J.S. Schuman, W.G. Stinson, W. Chang, M.R. Hee, T. Flotte, K. Gregory, C.A. Puliafito, and J.G. Fujimoto, "Optical coherence tomography," Science **254**, 1178-1181 (1991).

6. J. Elisseeff, K. Anseth, D. Sims, W. McIntosh, M. Randolph, and R. Langer, "Transdermal photopolymerization for minimally invasive implantation," Proc. Natl. Acad. Sci. USA **96,** 3104-3107 (1999).

7. M. R. Hee, D. Huang, E. A. Swanson, and J. G. Fujimoto, "Polarization-sensitive low-coherence reflectometer for birefringence characterization and ranging," J. Opt. Soc. Am. B **9**, 903-908 (1992).

8. J.F. de Boer, T.E. Milner, M.J.C. van Gemert, and J.S. Nelson, "Two-dimensional birefringence imaging in biological tissue by polarization-sensitive optical coherence tomography," Opt. Lett. **22**, 934-936 (1997).

9. M. Todorović, S. Jiao, L.V. Wang, and G. Stoica, "Determination of local polarization properties of biological samples in the presence of diattenuation by use of Mueller optical coherence tomography," Opt. Lett. **29**, 2402-2404 (2004).

10. C.K. Hitzenberger, E. Götzinger, M. Sticker, M. Pircher, and A.F. Fercher, "Measurement and imaging of birefringence and optic axis orientation by phase resolved polarization sensitive optical coherence tomography," Opt. Express **9**, 780-790 (2001).

11. E. Götzinger, M. Pircher, and C.K. Hitzenberger, "High speed spectral domain polarization sensitive optical coherence tomography of the human retina," Opt. Express **13**, 10217-10229 (2005).

12. R. Leitgeb, C.K. Hitzenberger, and A.F. Fercher, "Performance of Fourier domain vs. time domain optical coherence tomography," Opt. Express **11**, 889-894 (2003).

13. J.F. de Boer, B. Cense, B.H. Park, M.C. Pierce, G.J. Tearney, and B.E. Bouma, "Improved signal-to-noise ratio in spectral-domain compared with time-domain optical coherence tomography," Opt. Lett. **28**, 2067-2069 (2003).

14. J.F. de Boer, T.E. Milner, and J.S. Nelson, "Determination of the depth-resolved Stokes parameters of light backscattered from turbid media by use of polarization-sensitive optical coherence tomography," Opt. Lett. **24**, 300-302 (1999).

15. C.E. Saxer, J.F. de Boer, B.H. Park, Y. Zhao, Z. Chen, and J.S. Nelson, "High-speed fiber-based polarization-sensitive optical coherence tomography of *in vivo* human skin," Opt. Lett. **25**, 1355-1357 (2000).

16. J. Zhang, W. Jung, J.S. Nelson, and Z. Chen, "Full range polarization-sensitive Fourier domain optical coherence tomography," Opt. Express **12**, 6033-6039 (2004).

17. B. Cense, T.C. Chen, M. Mujat, C. Joo, T. Akkin, B.H. Park, M.C. Pierce, A. Yun, B.E. Bouma, G.J. Tearney, and J.F. de Boer, "Spectral-domain polarization-sensitive optical coherence tomography at 850 nm," Proc. of SPIE **5690**, 159-162 (2005).

18. G. Yao and L.V. Wang, "Two-dimensional depth-resolved Mueller matrix characterization of biological tissue by optical coherence tomography," Opt. Lett. **24**, 537-539 (1999).

19. Y. Yasuno, S. Makita, Y. Sutoh, M. Itoh, and T. Yatagai, "Birefringence imaging of human skin by polarization-sensitive spectral interferometric optical coherence tomography," Opt. Lett. **27**, 1803-1805 (2002).

20. S. Jiao and L.V. Wang, “Jones-matrix imaging of biological tissues with quadruple-channel optical coherence tomography,” J. Biomed. Opt. **7**, 350-358 (2002).

21. J.E. Roth, J.A. Kozak, S. Yazdanfar, A.M. Rollins, and J.A. Izatt, “Simplified method for polarization-sensitive optical coherence tomography,” Opt. Lett. **26**, 1069-1071 (2001).

22. S. Jiao, M. Todorović, G. Stoica, and L.V. Wang, “Fiber-based polarization-sensitive Mueller matrix optical coherence tomography with continuous source polarization modulation,” Appl. Opt. **44**, 5463-5467 (2005).

23. H.M. Jones, R.J. Baskin, and Y. Yeh, "The molecular origin of birefringence in skeletal muscle. Contribution of myosin subfragment S-1," Biophys. Jour. **60**, 1217-1228 (1991).

24. P. Whittaker and P.B. Canham, "Demonstration of quantitative fabric analysis of tendon collagen using two-dimensional polarized light microscopy," Matrix **11**, 56-62 (1991).

25. K. Gelse, E. Pöschl, and T. Aigner, “Collagens—structure, function, and biosynthesis,” Adv. Drug Del. Rev. **55,** 1531-1546 (2003).

26. J.J. Pasquesi, S.C. Schlachter, M.D. Boppart, E. Chaney, S.J. Kaufman, and S.A. Boppart, “In vivo detection of exercised-induced ultrastructural changes in genetically-altered murine skeletal muscle using polarization-sensitive optical coherence tomography,” Opt. Express **14**, 1547-1556 (2006).

27. J.J. Gil and E. Bernabeu, "Obtainment of the polarizing and retardation parameters of a non-depolarizing optical system from the polar decomposition of its Mueller matrix," Optik, **76**, 67-71 (1987).

28. G.J. Tearney, B.E. Bouma, and J.G. Fujimoto, "High-speed phase- and group-delay scanning with a grating-based phase control delay line," Opt. Lett. **22**, 1811-1813 (1997).

29. S. Jiao, W. Yu, G. Stoica, and L.V. Wang, "Optical-fiber-based Mueller optical coherence tomography," Opt. Lett. **28**, 1206-1208 (2003).

30. S. Jiao, G, Yao, and L.V. Wang, "Depth-resolved two-dimensional stokes vectors of backscattered light and Mueller matrices of biological tissue measured with optical coherence tomography," Appl. Opt. **39**, 6318-6324 (2000).

31. S. Jiao and L.V. Wang, "Two-dimensional depth-resolved Mueller matrix of biological tissue measured with double-beam polarization-sensitive optical coherence tomography," Opt. Lett. **27**, 101-103 (2002).

32. M.C. Pierce, B.H. Park, B. Cense, and J.F. de Boer, "Simultaneous intensity, birefringence, and flow measurements with high-speed fiber-based optical coherence tomography," Opt. Lett. **27**, 1534-1536 (2002).

33. H. Ren, Z. Ding, Y. Zhao, J. Miao, J.S. Nelson, and Z. Chen, "Phase-resolved functional optical coherence tomography: simultaneous imaging of in situ tissue structure, blood flow velocity, standard deviation, birefringence, and Stokes vectors in human skin," Opt. Lett. **27**, 1702-1704 (2002).

34. D.D. Streeter, *Handbook of Physiology: The Cardiovascular System*, (American Physiological Society, Bethesda, MD, 1979).

35. American Burn Association, "Burn Incidence and Treatment in the US: 2000 Fact Sheet," (2000), http://www.ameriburn.org/resources_factsheet.php.

36. R.S. Cotran, V. Kumar, and T. Collins, *Robbins Pathologic Bases of Disease*, (W.B. Saunders Co., Philadelphia, PA, 1999).

37. R.M. Johnson and R. Richards, "Partial-thickness burns: identification and management," Adv. Skin & Wound Care **16**, 178-187 (2003).

38. United States National Institutes of Health, *Guide for the Care and Use of Laboratory Animals*, (US Government Printing Office, Washington DC, 1985).

39. M.J. Escamez, M. García, F. Larcher, A. Meana, E. Muñoz, J.L. Jorcano, and M. Del Río, "An in vivo model of wound healing in genetically modified skin-humanized mice," J. Investig. Dermatol. **123**, 1182-1191 (2004).

40. National Cancer Institute, "Skin cancer," (2008), http://www.cancer.gov/cancertopics/types/skin.

41. A. Glaessl, A.G. Schreyer, M.B. Wimmershoff, M. Landthaler, S. Feuerbach, and U. Hohenleutner, "Laser surgical planning with magnetic resonance imaging–based 3-dimensional reconstructions for intralesional Nd:YAG laser therapy of a venous malformation of the neck," Arch. Dermatol. **137**, 1331-1335 (2001).

42. C.C. Harland, S.G. Kale, P. Jackson, P.S. Mortimer, and J.C. Bamber, "Differentiation of common benign pigmented skin lesions from melanoma by high-resolution ultrasound," B. J. Dermatol. **137**, 281-289 (2000).

43. T. Stepinac, C. Felley, P. Jornod, N. Lange, T. Gabrecht, C. Fontolliet, P. Grosjean, G. van Melle, H. van den Bergh, P. Monnier, G. Wagnières, and G. Dorta, "Endoscopic fluorescence detection of intraepithelial neoplasia in Barrett's esophagus after oral administration of aminolevulinic acid," Endoscopy **35**, 663-668 (2003).

44. Y.T. Pan, T.Q. Xie, C.W. Du, S. Bastacky, S. Meyers, and M.L. Zeidel, "Enhancing early bladder cancer detection with fluorescence-guided endoscopic optical coherence tomography," Opt. Lett. **28**, 2485-2487 (2003).

45. M. Motamedi, R. Johnigan, B. Bell, J. Pasricha, and K. Calhoun, "Fluorescence guided optical coherence tomography for early detection of epithelial neoplasia," Proc. of Lasers and Electro-Optics Society 2000 Annual Meeting **1**, 151 (2000).

46. A. Garcia-Uribe, N. Kehtarnavaz, G. Marquez, V. Prieto, M. Duvic, and L.V. Wang, "Skin cancer detection by spectroscopic oblique-incidence reflectometry: classification and physiological origins," App. Opt. **43**, 2643-2650 (2004).

47. T. Yamashita, K. Negishi, T. Hariya, N. Kunizawa, K. Ikuta, M. Yanai, and S. Wakamatsu, "Intense pulsed light therapy for superficial pigmented lesions evaluated by reflectance-mode confocal microscopy and optical coherence tomography," J. Investig. Dermatol. **126**, 2281-2286 (2006).

48. J. Strasswimmer, M.C. Pierce, B.H. Park, V. Neel, and J.F. de Boer, "Polarization-sensitive optical coherence tomography of invasive basal cell carcinoma," J. Biomed. Opt. **9**, 292-298 (2004).

49. T.J. Slaga, "SENCAR mouse skin tumorigenesis model versus other strains and stocks of mice," Environ. Health Perspect. **68**, 27-32 (1986).

50. D.C. Montgomery, E.A. Peck, and G.G. Vining, *Introduction to Linear Regression Analysis*, (John Wiley & Sons, New York, NY 2001).

51. M.E. Brezinski, G.J. Tearney, B.E. Bouma, J.A. Izatt, M.R. Hee, E.A. Swanson, J.F. Southern, and J.G. Fujimoto, "Optical coherence tomography for optical biopsy: properties and demonstration of vascular pathology," Circ. Amer. Heart Assoc. **93**, 1206-1213 (1996).

52. T.J. Slaga, J. DiGiovanni, L.D. Winberg, and I.V. Budunova, "Skin carcinogenesis: characteristics, mechanisms, and prevention," in *Growth Factors and Tumor Promotion: Implications for Risk Assessment*, R.M. McClain, T.J. Slaga, R. LeBoeuf, and H. Pitot, ed. (Wiley-Liss, 1993).

53. D. Pereda-Cubián, M. Todorović, J.L. Arce-Diego, and L.V. Wang, "Evaluation of the magneto-optical effect in biological tissue models using optical coherence tomography," J. Biomed. Opt. Lett. **12**, 060502−1-3 (2007).

VITA

Milos Todorovic received his Bachelor of Science (Diploma Engineer) degree in electrical engineering with concentration in telecommunications and signal processing from the University of Belgrade, Serbia in 1999, and his Master of Science degree in Electrical Engineering from Texas A&M University in College Station, TX in 2002. He entered the Biomedical Engineering program at Texas A&M University in 2003 and received his Doctor of Philosophy degree in August of 2008. His research interests are in the medical imaging field with a focus on non-ionizing, non-invasive, high-resolution optical modalities.

Milos Todorovic can be reached through the Department of Biomedical Engineering, Texas A&M University, TAMU 3120, College Station, TX 77843-3120. His email address is todorovic.milos @ gmail.com.